Shear wave velocity structure at the Fukushima forearc region based on H/V analysis of ambient noise recordings by ocean bottom seismometers

Atikul Haque Farazi [1,2] Yoshihiro Ito [3] Emmanuel Soliman M. Garcia [3] Agostiny Marrios Lontsi,[4,5] Francisco José Sánchez-Sesma,[6] Aristoteles Jaramillo,[6] Shukei Ohyanagi,[1] Ryota Hino[7] and Masanao Shinohara[8]

[1]*Division of Earth and Planetary Sciences, Kyoto University, 611-0011, Kyoto, Japan. E-mail: farazi.haque.38w@st.kyoto-u.ac.jp*
[2]*Department of Geology and Mining, University of Barishal, 8254, Barishal, Bangladesh*
[3]*Disaster Prevention Research Institute (DPRI), Kyoto University, 611-0011, Uji, Kyoto, Japan*
[4]*Swiss Seismological Service (SED), ETH Zürich, 8092, Zürich, Switzerland*
[5]*Department of Civil and Architectural Engineering, Faculty of Engineering and Technology, University of Buea, 63, Buea, Cameroon*
[6]*Instituto de Ingeniería CU, Universidad Nacional Autónoma de México, 04510, CDMX, Mexico*
[7]*Research Center for Prediction of Earthquakes and Volcanic Eruptions, Tohoku University, 8577, Miyagi, Japan*
[8]*Earthquake Research Institute, University of Tokyo, 113-8654, Tokyo, Japan*

SUMMARY

This study presents the shear wave velocity (V_S) structures of sedimentary sequences and a section of the upper crustal layer in the Fukushima forearc region of the Japan Trench subduction zone, which were obtained by analysing the horizontal-to-vertical (H/V) spectral ratios of ambient vibration records. The H/V curves were derived using 31 d of continuous seismic data from 3 broad-band and 16 short-period ocean bottom seismometer (OBS) stations. Using the broad-band data, H/V ratios from 0.01 to 10 Hz were derived, but the ratios below 0.1 Hz frequencies were unusually large and temporally unstable. Characterization of seismic noise energy from ∼1 yr of seismic data of three broad-band OBSs revealed variable and elevated energy conditions below 0.1 Hz due to typical long-period oceanic noise; we link these observations with the unstable H/V ratios below this frequency. Therefore, H/V analysis was performed in the frequency range of 0.1–10 Hz for both broad-band and short-period OBSs to obtain subsurface V_S profiles. For the forward calculation of the H/V ratios in the inversion process, we used the recently developed 'hvgeneralized' method, which is based on the diffuse field assumption, and accounts for the water layer on top of stratified media. Moreover, available prior geological and geophysical information was utilized during the inversion of the H/V curves. We found that subsurface V_S ranged from approximately 30 m s^{-1} at the seabed to approximately 4900 m s^{-1} at 7000 m below the sea floor (mbsf). Starting with the best model candidate at each OBS location, the effect of the water layer on the H/V curve in the deep ocean was investigated by comparing synthetic H/V curves with and without the water layer. The synthetic H/V analysis revealed that the water layer had a significant effect on H/V amplitudes at higher frequencies (>1 Hz), whereas comparatively little effect was observed at lower frequencies (<1 Hz). This study provides an empirical basis for H/V analysis using OBS data to determine V_S down to several kilometres of sedimentary sequences to the upper crust with high-resolution.

Key words: Japan; Seismic noise; Crustal structure; Full H/V inversion; Shear-wave velocity.

1 INTRODUCTION

Seismic ambient noise (SAN) or ambient vibration is generated by natural causes that induce microseisms with frequencies generally smaller than 1 Hz, such as oceanic waves (Ardhuin *et al.* 2011), or by human activities that generate microtremors with frequencies generally greater than 1 Hz, such as industry and traffic (Webb 1998; Fäh *et al.* 2001; Bonnefoy-Claudet

et al. 2006a; Nishida 2017; Rahman *et al.* 2018; Nakata *et al.* 2019; Lecocq *et al.* 2020; Ba *et al.* 2021). Exploiting the wide frequency range of the SAN wavefield is a time- and cost-effective approach for obtaining the subsurface shear (*S*)-wave velocity (V_S) profile over a broad depth range (Horike 1985; Tokimatsu *et al.* 1992; Asten & Boore 2005; Bard *et al.* 2010; Lontsi *et al.* 2015; Bao *et al.* 2018; Perton *et al.* 2020; Molnar *et al.* 2022).

Subsurface imaging methods using ambient seismic noise data can be divided into array-based and single-station techniques. Array techniques to determine V_S structure through inversion include the determination of surface wave dispersion curves using spatial autocorrelation (SPAC; Aki 1957), frequency–wavenumber analysis (*f*-k; Lacoss *et al.* 1969; Poggi & Fäh 2010), interferometric multi-channel analysis of surface waves (IMASW; Lontsi *et al.* 2016) and wavefield decomposition (WaveDec, Maranò *et al.* 2012), among others. Surface wave tomography can also be performed using cross-correlation of SAN array recordings (Picozzi *et al.* 2005; Shapiro *et al.* 2005; Bensen *et al.* 2007; Hannemann *et al.* 2014). In contrast, using single-station methods, the V_S profile can be obtained from the inversion of the Rayleigh wave ellipticity (Yamanaka *et al.* 1994; Fäh *et al.* 2003; Arai & Tokimatsu 2004) or full horizontal-to-vertical (H/V) ratio spectrum (Lontsi *et al.* 2015). Notably, the H/V spectral ratio is sensitive to vertical changes in V_S at the subsurface, whereas tomographic methods are sensitive to spatial variations in V_S (Perton *et al.* 2020).

In this study, we worked with the single-station H/V method. The technique has been widely used over the past decades since its introduction by Nogoshi & Igarashi (1971), particularly for seismic site characterization through investigation of subterranean V_S structure (Fäh *et al.* 2001; Arai & Tokimatsu 2004; Picozzi *et al.* 2005; Pilz *et al.* 2010; Lontsi *et al.* 2015; Piña-Flores *et al.* 2017; Sánchez-Sesma 2017; Wu *et al.* 2017; Spica *et al.* 2018; Bora *et al.* 2020; Farazi *et al.* 2023), site response estimation from resonance frequency (Nakamura 1989, 2000; Lermo & Chávez- García 1993; Huerta- López *et al.* 2003; Bonnefoy-Claudet *et al.* 2006b; Nakamura 2008; Hellel *et al.* 2012; Vella *et al.* 2013; Qadri *et al.* 2015; Rahman *et al.* 2018), and determination of sediment thickness overlying the bedrock (Nakamura 2000; Hellel *et al.* 2012; Manea *et al.* 2020; Rahman *et al.* 2021). This approach is generally used to investigate shallow depths (∼200 m) (Nakamura 1989), but it has also been successfully employed for intermediate (∼2000 m) (Asten *et al.* 2014) and greater depths (several thousand metres; Perton *et al.* 2020).

Despite its capability in providing reliable site information, the wavefield composition of the H/V spectral ratio curve remains complex. Considering that SAN is a diffuse field, Sánchez-Sesma *et al.* (2011) proposed the following interpretation of the H/V spectral ratio: within a diffuse field, the directional energy densities (DEDs) are proportional to the imaginary parts of the Green's function (GF) when both the source and receiver coincide (Sánchez-Sesma *et al.* 2008). Therefore, the diffuse field assumption (DFA) allows for the linking of the H/V ratio described by Nakamura (1989) with the square root of the H/V ratios of the imaginary parts of the GF. This new framework for H/V spectral ratio calculation does not suffer any limitations regarding the wave types that constitute the noise wavefield, but it does require diffuse field condition. The latter is not always achieved in practice; however, its characteristics can likely be evaluated through temporal and azimuthal variation studies prior to performing the inversion. Depending on the approach used to calculate the GF, the body, Rayleigh and Love-wave contributions to the H/V spectral ratio can be intrinsically accounted for either

collectively (Sánchez-Sesma *et al.* 2011; Lontsi *et al.* 2015) or separately (García-Jerez *et al.* 2016). The latest physical development involves the H/V calculations at boreholes and in offshore environments, where the presence of the water layer is explicitly accounted for (Lontsi *et al.* 2019).

Compared to the wide application of the H/V method onshore, the offshore application is limited. The first well-known effort was made by Huerta-López *et al.* (2003), followed by Muyzert (2007), Overduin *et al.* (2015), Shynkarenko *et al.* (2021). In this study, we extended the use of the 'hvgeneralized' algorithm (Lontsi *et al.* 2019) to investigate the subsurface V_S profile (extending up to 7000 m underground) of well-defined deep structures in the offshore Fukushima forearc region (Fig. 1).

SAN-based observation and monitoring by OBSs in oceanic environments can be complicated at low frequencies (<0.1 Hz) because of contamination of the recorded waveforms by waves other than the seismic noise that propagates through the earth. Such waves could include gravity waves on the horizontal components (Beauduin *et al.* 1996; Webb 1998; Angelis & Bodin 2012; Raspet *et al.* 2022). However, recordings at lower frequencies are required to increase the depth of observation. Therefore, we compute the power spectral densities (PSDs; McNamara and Buland 2004) to characterize noise levels at three broad-band OBS stations and to determine a stable frequency range for H/V analysis. The noise levels were characterized by probabilistic power spectral density (PPSD) analysis, which are probability density functions (PDFs) of PSDs.

The offshore Fukushima region was previously studied by the Japan Agency for Marine Science and Technology (JAMSTEC) during the KR98 active-source seismic survey (Tsuru *et al.* 2002; Miura *et al.* 2003; JAMSTEC 1998) to estimate *P*-wave velocity in deep subsurface structures. Several authors evaluated both the V_P and V_S structures of this region, for the maximum depth range of 700 km down to the subsurface, using passive methods (Huang *et al.* 2011; Liu & Zhao 2016). Moreover, the Japan Geological Survey (JGS) conducted a high-resolution reflection survey using a sub-bottom profiler (SBP) to determine very shallow (≤100 m from the ocean bottom) subsurface structures in this area (https://gbank.gsj. jp/sbp_db/812-3html/PAGES/812-3E.html). However, none of the previous studies presented V_S information for sedimentary layers other than the average velocity of the upper crust.

Despite the importance of marine sediment V_S information in seismology and marine exploration, among other applications (Yamaya *et al.* 2021), it is generally not well constrained. The requirement of sufficient energy conversion to produce substantial *S*-wave phases limits investigations using active-source seismic surveys (Ruan *et al.* 2014). Owing to this limitation, Scholte-wave tomography can only consider depths of <100 m (e.g. Kugler *et al.* 2007). This study provides a detailed evaluation of V_S from below the seabed to the upper crust using H/V analysis of SAN, with specific reference to the DFA. We also evaluated the effect of the water layer on the observed H/V curve using synthetic H/V analysis.

2 STUDY AREA AND TECTONIC SETTING

The offshore Fukushima forearc region in northeast Japan is adjacent to the southern extension of the Japan Trench (Miura *et al.* 2003) in the northwest Pacific Ocean, along which the oceanic Pacific Plate subducts beneath the continental Okhotsk Plate at a convergence rate of around 7.5–10 cm yr^{-1} (Apel *et al.* 2006; Altamimi *et al.* 2007) (Fig. 1a). The westernmost extent of our study
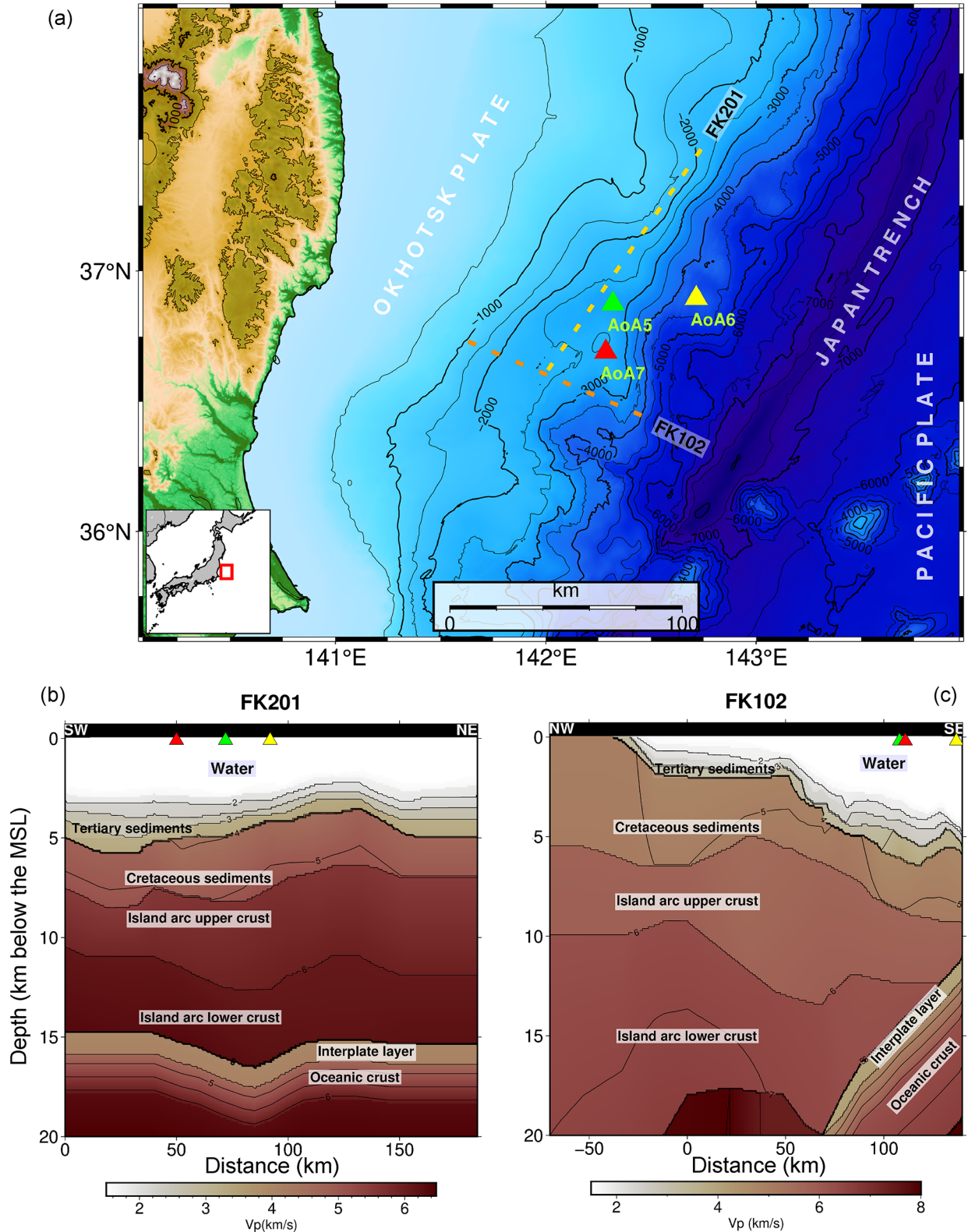
Figure 1. (a) Map of the major tectonic elements in and around offshore Fukushima, Japan (Hua *et al.* 2020). (b) 2D V_P profile of parallel (FK201 in [a]) and (c) perpendicular trench axes (FK102 in [a]), reproduced from Miura *et al.* (2003), but only for 20 km below mean sea level (MSL), representing the major subsurface structures. The relative positions of AoA5, AoA6 and AoA7 are shown by solid green, yellow and red triangles, respectively, in (b) and (c). The area filled with black colour at the top of both (b) and (c) represents the air above the MSL.

area is ∼140 km east of the shoreline and the easternmost periphery is ∼40 km west of the Japan Trench axis. The OBSs are distributed within 36.690° to 36.900° N and 142.282° to 142.719° E, where the seabed depth varies from approximately 2520 to 4280 m below mean sea level (MSL, Fig. 1a). The plate interface is relatively shallow (∼7 to ∼12 km from the east to the west) (Miura *et al.* 2003) with remarkably less seismicity (Nishikawa *et al.* 2019) compared to the offshore Tohoku region further north along the Japan Trench (Miura *et al.* 2003); nevertheless, relatively high tectonic tremor activities or slow earthquakes have been reported (Ohta *et al.* 2019), which may be explained by the subsurface seismic structure around the plate interface. Using the active air gun survey results of Tsuru *et al.* (2002, JAMSTEC (1998), see Figs 9 and 13) and Miura *et al.* (2003, see Figs 4a and 10a) described the crustal structure of this area in terms of compressional wave (*P*-wave) velocity (V_P) modelling. These studies showed that there are three major layers from the seabed to the upper crust of the study area: (i) Tertiary sedimentary sequences (2000–3000 m thick), (ii) Cretaceous sedimentary sequences (2000–3000 m thick) and (iii) island arc upper crust (2000–3000 m thick) (Figs 1b and c). This survey area falls well within our study area (shown by the trench axis parallel and perpendicular survey lines FK201 and FK102, respectively, in Fig. 1a) and allows for an informed interpretation of our results (Figs 1b and c).

3 DATA

A total of 19 three-component OBSs were used, three of which were broad-band seismometers (Guralp CMG-3T-360) and the rest of which were short-period seismometers (Guralp CMG-40T-1). Broad-band seismometers have a flat response from 0.02 to 360 s (0.003 to 50 Hz), and short-period seismometers have a flat response from 0.02 to 1 s (1 to 50 Hz). The sampling frequency for both type of sensors was 200 Hz. Three arrays, namely AoA5, AoA6 and AoA7 (Figs 1a and 2), were deployed by free-fall from the sea surface to the seabed. Each array had one broad-band seismometer and six short-period seismometers (Fig. 2). The stations in each array were numbered from 0 (broad-band station in all arrays) to 6, for example AoA50 (broad-band), AoA51, AoA52, AoA53, AoA54, AoA55 and AoA56. Among them, two short-period seismometers (AoA54 and AoA61) were not used because of poor data quality.

4 METHODS

4.1. H/V estimation

For each OBS station, the H/V curve was computed using 31 d (25–09-2016 to 26–10-2016) of continuous seismic data. H/V curves were computed using the broad-band OBSs between 0.01 and 10 Hz to retrieve deep subsurface information (Fig. 3). However, we found that the H/V ratios were temporally unstable with unusually large amplitudes at frequencies below 0.1 Hz, whereas they were stable above 0.1 Hz (Fig. 3). Using all OBSs, H/V curves within the 0.1 to 10 Hz frequency range were derived; they showed satisfactory spatial stability among the stations of each array (Fig. 4). Therefore, we only considered frequencies between 0.1 and 10 Hz and proceeded to invert the H/V curves to obtain the underground V_S profile at each station.

In this study, we considered the horizontal spectrum of the H/V curve to be the square root of the sum of the squared horizontal components. To properly use the SAN recordings, we removed the

mean and trend from the data and applied tapering and appropriate filtering. We used Geopsy software (Wathelet *et al.* 2020) to obtain the H/V curve. To remove energetic signals from the SAN data and improve the reliability of the measured H/V spectra, the average amplitude ratio algorithm was applied with a short-time to long-time window (STA/LTA). Furthermore, the Konno–Ohmachi smoothing algorithm (Konno & Ohmachi 1998), with a smoothing constant set to 40, was applied to the Fourier amplitude spectrum of each component.

The azimuthal variation of the H/V ratios for all the OBSs was also evaluated by rotating the north–south (NS) and east–west (EW) components from 0° (north) to 180° (south) in increments of 10° (Fig. 5 and Supplementary Fig. S1). We did not attempt to correct the orientation of the OBS sensors so that the wavefields and the H/V amplitudes were similar to those for the H/V ratios used in the inversion (Fig. 4). The results are plotted showing the H/V amplitude as a function of frequency (x axis) versus azimuth (y axis). Among the higher frequencies, some directionality was observed around the peak frequencies; an interpretation of this result was outside the scope of this study.

4.2 Noise level estimation

SAN energy levels at three broad-band OBSs were characterized with an emphasis on investigating the reason behind the unstable H/V ratios at low frequencies (< 0.1 Hz) in the oceanic environment. Nearly one year of recordings (from 2016 September 25 to 2017 September 15) from three broad-band OBS stations (AoA50, AoA60 and AoA70) were used to estimate the SAN energy variations. We applied the method of McNamara and Buland (2004), implemented in ObsPy (Beyreuther *et al.* 2010), which utilizes PSDs and PDFs to characterize SAN energy through PPSD analysis. The PSDs were used to define the PDFs of the noise and were computed using the algorithm proposed by Peterson (1993).

The PSD curves represent the energy density per unit time as a function of frequency (Vassallo *et al.* 2012). For PSD estimation, velocity time-series data were segmented into 1-hr segments with a 50 percent overlap. Each 1-hr segment was further divided into 13 segments with 75 percent overlap. Mean and trend removal as well as tapering was applied to each segment. Subsequently, the Fourier amplitude spectrum was obtained for each segment. Then, the squared amplitude of each frequency sample of the amplitude spectrum was normalized by a factor of $2\Delta t/N$, that is twice the ratio of the sample interval (Δt) to the number of samples (N). Thus, a PSD curve was obtained for every segment. Finally, a 1-hr PSD was constructed by averaging the 13 PSD segments. The PSD estimate was then converted to decibels (dB) with respect to acceleration ($[\text{m s}^{-2}]^2$/Hz). To obtain the PDF, each PSD curve was smoothed by grouping full octave averages, centred on octave windows at 1/8-octave intervals, into 1-dB bins. For a comprehensive evaluation of the noise levels as well as the features of the noise spectra and their sources, we conducted a PPSD analysis based on the PDF mode of the PSDs (Fig. 6 and Supplementary Fig. S2).

The features of oceanic noise, that is the primary and secondary peaks on all the components, and the higher frequency shear mode peaks on the horizontal components were clearly visible in our data set, including the unstable noise conditions at lower frequencies (<0.1 Hz). Similar observations have been reported in several other studies (e.g. Webb 1998; Crawford & Webb 2000; Dolenc *et al.* 2007; Angelis & Bodin 2012; Ardhuin *et al.* 2015; Tian & Ritzwoller 2015; Nishida 2017; Tian & Ritzwoller 2017). The PSDs
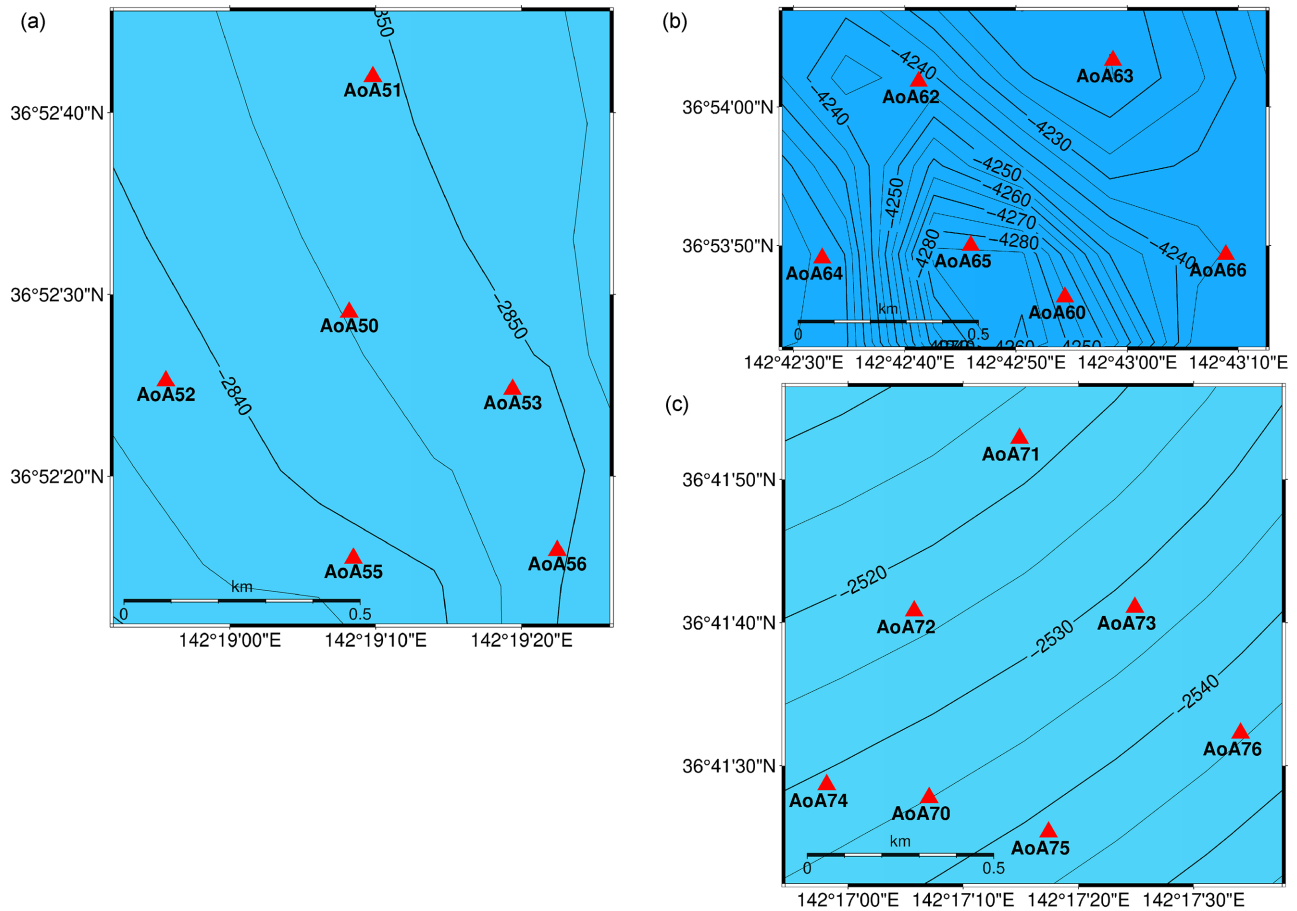
Figure 2. (a), (b) and (c) show the distribution of OBS stations at the array locations of AoA5, AoA6 and AoA7, respectively. The solid-red triangles indicate the sensor locations, where AoA50, AoA60 and AoA70 are the broad-band stations. Contour lines represent seabed elevations with respect to the MSL (m).
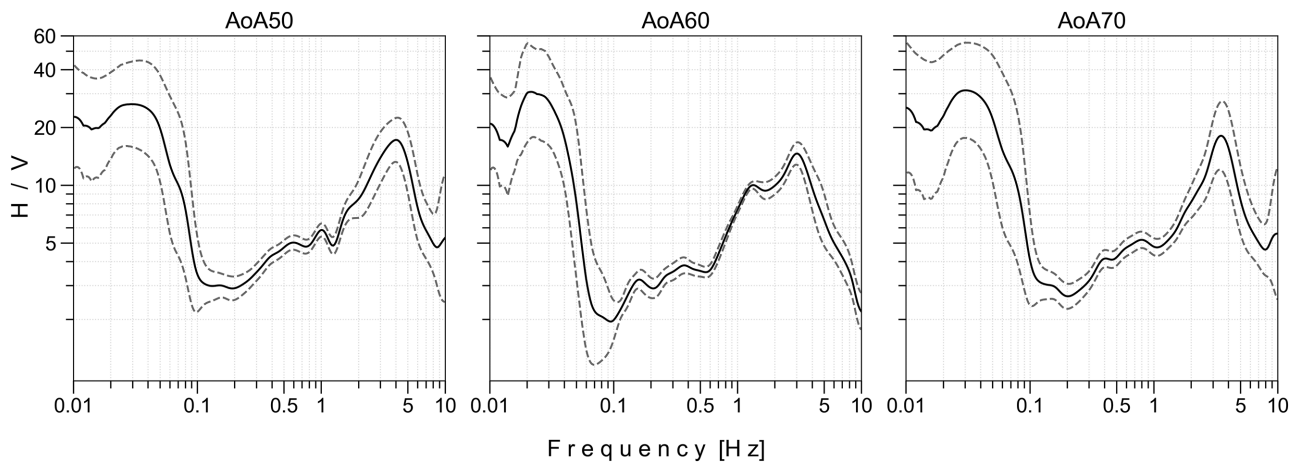
Figure 3. H/V curves from three broad-band stations (AoA50, AoA60 and AoA70 from left to right) within a range of 0.01 to 10 Hz. The high standard deviation values below 0.1 Hz indicate the unstable H/V ratios. The average H/V curve is represented by a solid black line, and the standard deviation is represented by a dashed grey line.

and noise modes within 0.1 to 10 Hz exhibited stable behaviour. Moreover, they were usually within the globally expected new high noise model (NHNM) and new low noise model (NLNM) of Peterson (1993). PSDs below 0.1 Hz showed increasing energy variation with decreasing frequency as well as at least a 20 dB higher energy level in the horizontal compared to vertical components (Fig. 6 and Supplementary Fig. S2). Such SAN energy conditions below 0.1 Hz

are indicative of increased noise and could be related to unstable H/V ratios (see Section 5.2.1). It should be noted that the lower frequency noises did not originate from the instruments: the flat frequency response of the broad-band OBSs was 0.003–50 Hz, and the self-noise was well below the NLNM. A detailed discussion of the observed noise characteristics in the study area between the frequencies 0.01 to 10 Hz is included in Section 5.2.
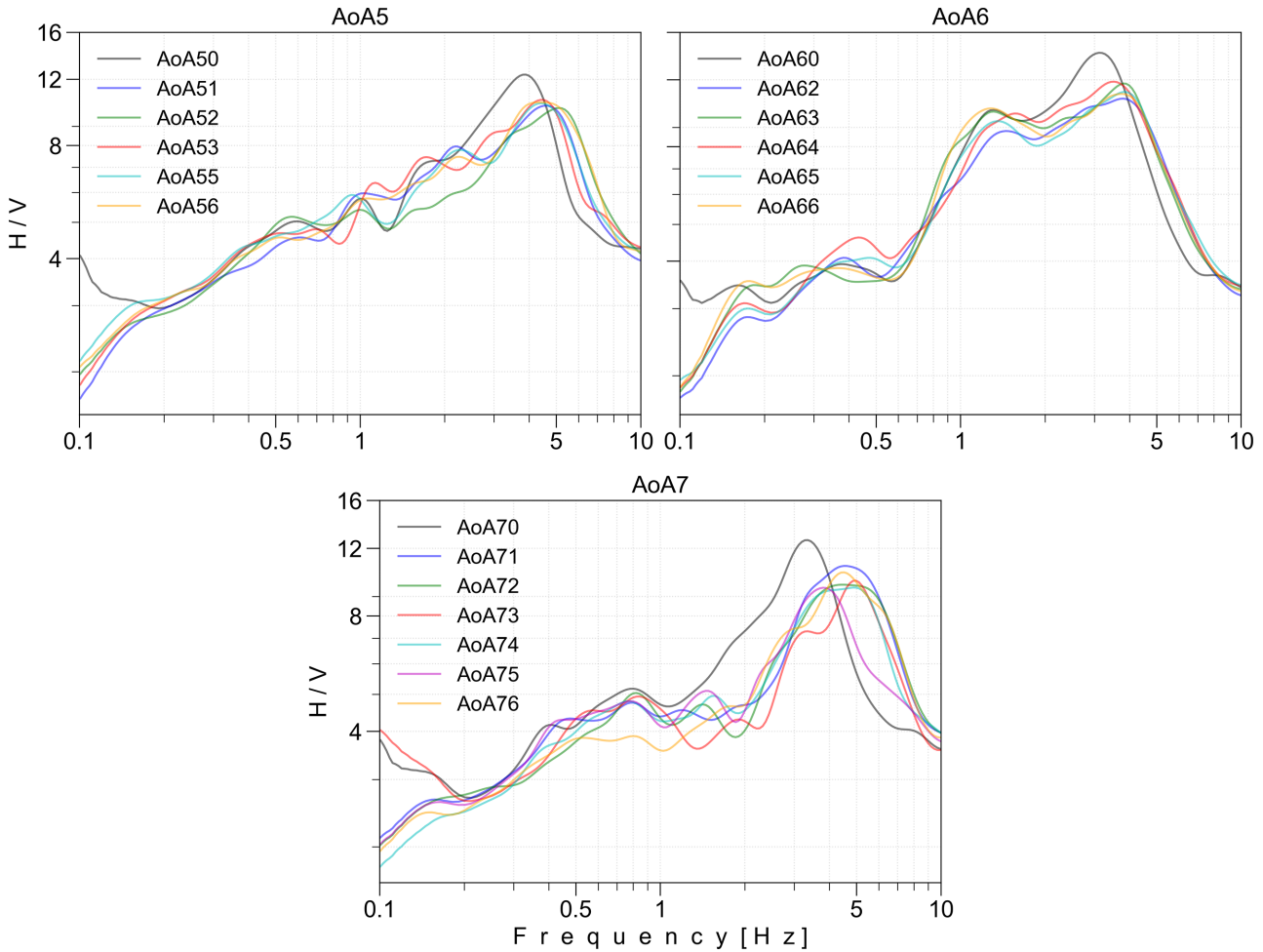
Figure 4. H/V curves for every OBS station at each array location (entitled on top of each panel).

4.3. H/V inversion

4.3.1 Forward modelling

Here, we applied the diffuse field theory and a recently developed H/V ratio forward computation algorithm, namely 'hvgeneralized' (Lontsi *et al.* 2015; Lontsi *et al.* 2019), in the inversion procedure. The 'hvgeneralized' algorithm accounts for Scholte, Love and multiple reflected body waves that constitute the noise wavefield under the assumption that the SAN wavefield is diffused. The diffuse field theory allows one to relate the energy measurements and their ratios with their elastodynamic counterparts and, consequently, determine the structure at depth. This theory also asserts that the motion autocorrelation within a diffuse field in the frequency domain is proportional to the imaginary part of the GF when both the source and receiver are colocated. Thus, the H/V spectral ratio can be interpreted in terms of the imaginary part of the GF (Sánchez-Sesma *et al.* 2011):

$$\frac{H}{V}(x, \omega) = \sqrt{\frac{E_1(x, \omega) + E_2(x, \omega)}{E_3(x, \omega)}} = \sqrt{\frac{Im(G_{11} + G_{22})}{Im(G_{33})}}, \quad (1)$$

where E_1, E_2 and E_3 are the DEDs, subscripts 1 and 2 refer to the horizontal degrees of freedom and subscript 3 refers to the vertical degrees of freedom.

For a diffuse, equipartitioned and harmonic displacement field component $u_i(x, \omega)$ within an elastic medium, the average cross-correlation of motions at points x_A and x_B can be expressed as (Sánchez-Sesma *et al.* 2008; Perton *et al.* 2009):

$$\langle u_i(\boldsymbol{x}_A, \omega) u_j^*(\boldsymbol{x}_B, \omega) \rangle \propto Im\left[G_{ij}(\boldsymbol{x}_A, \boldsymbol{x}_B, \omega)\right], \quad (2)$$

where $\omega = 2\pi f$ is the angular frequency, $u_i(x_A, \omega)$ is the displacement field component in the i direction at point $\boldsymbol{x}_A$ and $G_{ij}(\boldsymbol{x}_A, \boldsymbol{x}_B, \omega)$ is the GF. In this context, it means displacement in the i direction at point x_A caused by a unit harmonic point force at x_B in the j direction. The asterisk ($*$) indicates the complex conjugate so that the product is the cross-correlation in frequency domain, and the angular brackets ($\langle \rangle$) indicate the azimuthal or ensemble average.

When both source and receiver coincide, that is $\boldsymbol{x}_A = \boldsymbol{x}_B = \boldsymbol{x}$, the product is the autocorrelation in the frequency domain, and the DED in the direction m at point $\boldsymbol{x}$ can be written as (Sánchez-Sesma *et al.* 2008; Perton *et al.* 2009):

$$E_m(\boldsymbol{x}_A) = \rho\omega^2 \langle u_m(\boldsymbol{x}_A) u_m^*(\boldsymbol{x}_A) \rangle \propto Im\left[G_{mm}(\boldsymbol{x}_A, \boldsymbol{x}_A, \omega)\right], \quad (3)$$

where ρ is the mass density. Here, the summation convention is not applied.

In the 'hvgeneralized' algorithm, the energy contribution from the 1-D water layer above the seabed is considered in terms of a propagator matrix that accounts for both the in-plane polarization
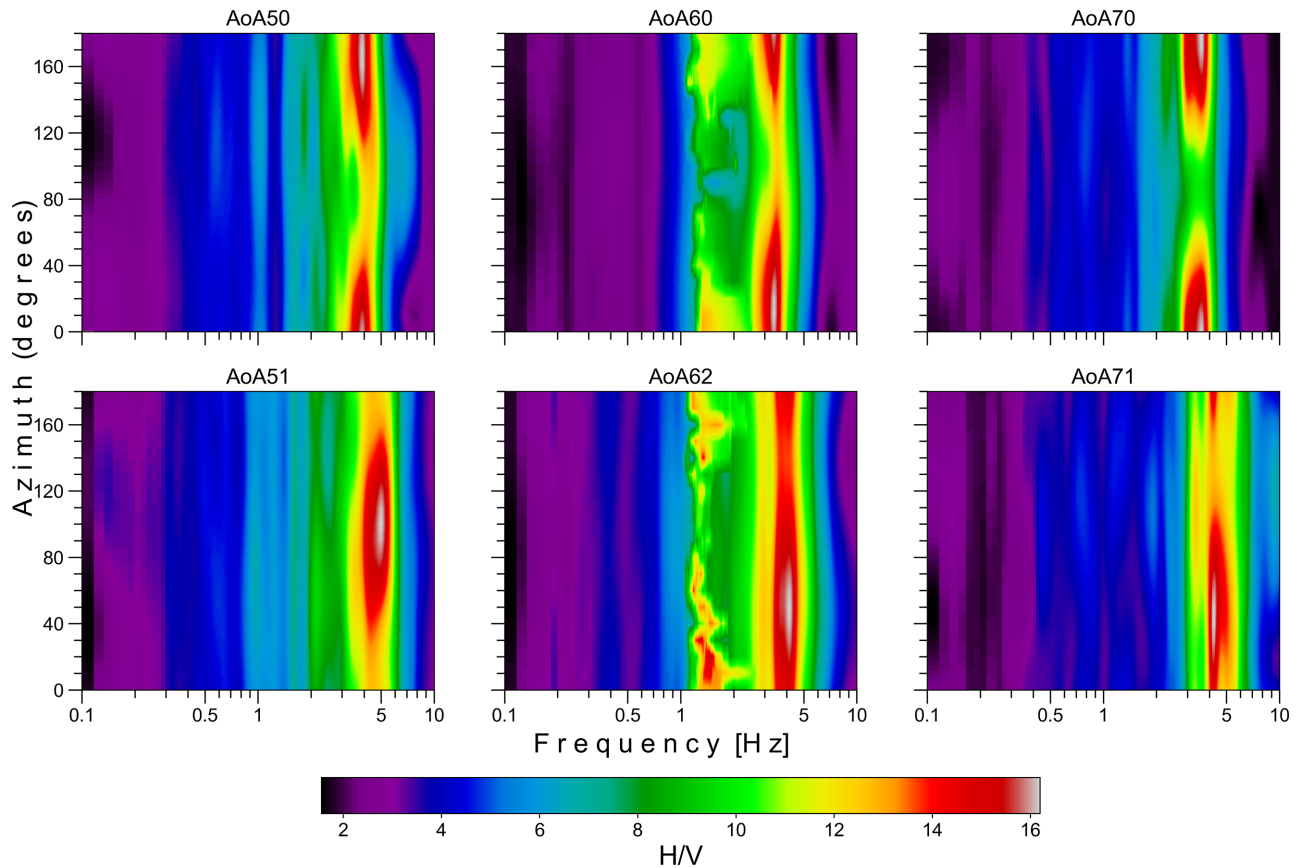
Figure 5. Representative azimuthal variation analysis results of H/V ratios for each array location, that is OBSs AoA50 (broadband) and AoA51 of array AoA5 (left-hand column); OBSs AoA60 (broadband) and AoA62 of array AoA6 (middle column); and OBSs AoA70 (broadband) and AoA71 of array AoA7 (right-hand column). Azimuthal variation analysis results of the H/V ratios for the remaining stations are presented in Supplementary Fig. S1.

of P-SV waves and the scalar nature of acoustic wave propagation within the fluid. However, the SH waves and water layer are uncoupled. In Lontsi *et al.* (2019), the corresponding kernels are computed using normalized Thomson–Haskell propagators (Thomson 1950; Haskell 1953) in terms of the horizontal wave number and numerically integrated to yield the desired imaginary parts of Green's tensor.

4.3.2 Sampling the parameter space

The inversion procedure requires four parameters per layer: thickness (h), V_P, V_S and mass density (ρ). Here, the Q-factor values for attenuation are ignored, assuming perfect elastic media. Density is not sensitive to this inversion; hence, an equal range is set for each layer (Lontsi *et al.* 2015). The setting of the initial parameter space takes advantage of the prior subsurface information.

When inverting the H/V curves, non-uniqueness was addressed by placing constraints on the inversion of the thickness of the layers in the parametrization, considering prior information on the subsurface layers obtained from various sources. For example, the active *P*-wave survey results by Miura *et al.* (2003) (Fig. 1a) provided information about shallow to deep structures (Figs 1b and c) with 100-m vertical intervals. Additionally, the shallow layers (<100 m) were classified according to the subsurface information from the SBP survey results of the JGS (https://gbank.gsj.jp/sbp_db/812-3h tml/PAGES/812-3E.html) and the Ocean Drilling Program at the Japan Trench off northeast Japan (Shipboard Scientific Party 2000).

The SBP survey provides information only on layer thickness (up to 100 m of the subsurface), while the ocean drilling data provides information on both layer thickness and V_P (up to 1200 m of the subsurface).

The minimum number of layers can be selected by visual appraisal of the number of peaks in the H/V spectra (Piña-Flores *et al.* 2017), along with the available subsurface information. The lower frequency portions, particularly below 1 Hz, generally originated from deeper layers. Perton *et al.* (2020) identified a peak near 0.2 Hz that was related to a structure at a depth of ~6 km in the Los Angeles Basin. The first-order approximation of the thickness of the shallower layers was performed following the well-known equations $f_o = \frac{V_s}{4h}$ (Nakamura 2000; Molnar *et al.* 2022) and $f_n = \frac{V_s}{4h}(2n+1)$ (Tuan *et al.* 2016), where n ($=0, 1, 2, ...$) is the mode number, f_n is the frequency of a peak in the H/V spectrum and h is the thickness. Based on forward modelling (details not shown) combined with the aforementioned prior shallow subsurface information, five to six layers were assumed for the Tertiary sedimentary sequences. Based on Miura *et al.* (2003) (also see Figs 1b and c), we did not assume any interlayer for the two deeper layers studied here, that is Cretaceous sedimentary sequences and the island arc upper crust.

Reference V_P information from shallow to deep subsurface in and around the study area are available from drilling data (Shipboard Scientific Party 2000), JAMSTEC (1998) and Huang *et al.* (2011). Relevant V_s information is available from Huang *et al.* (2011), and Liu & Zhao (2016) but they only include an average velocity for
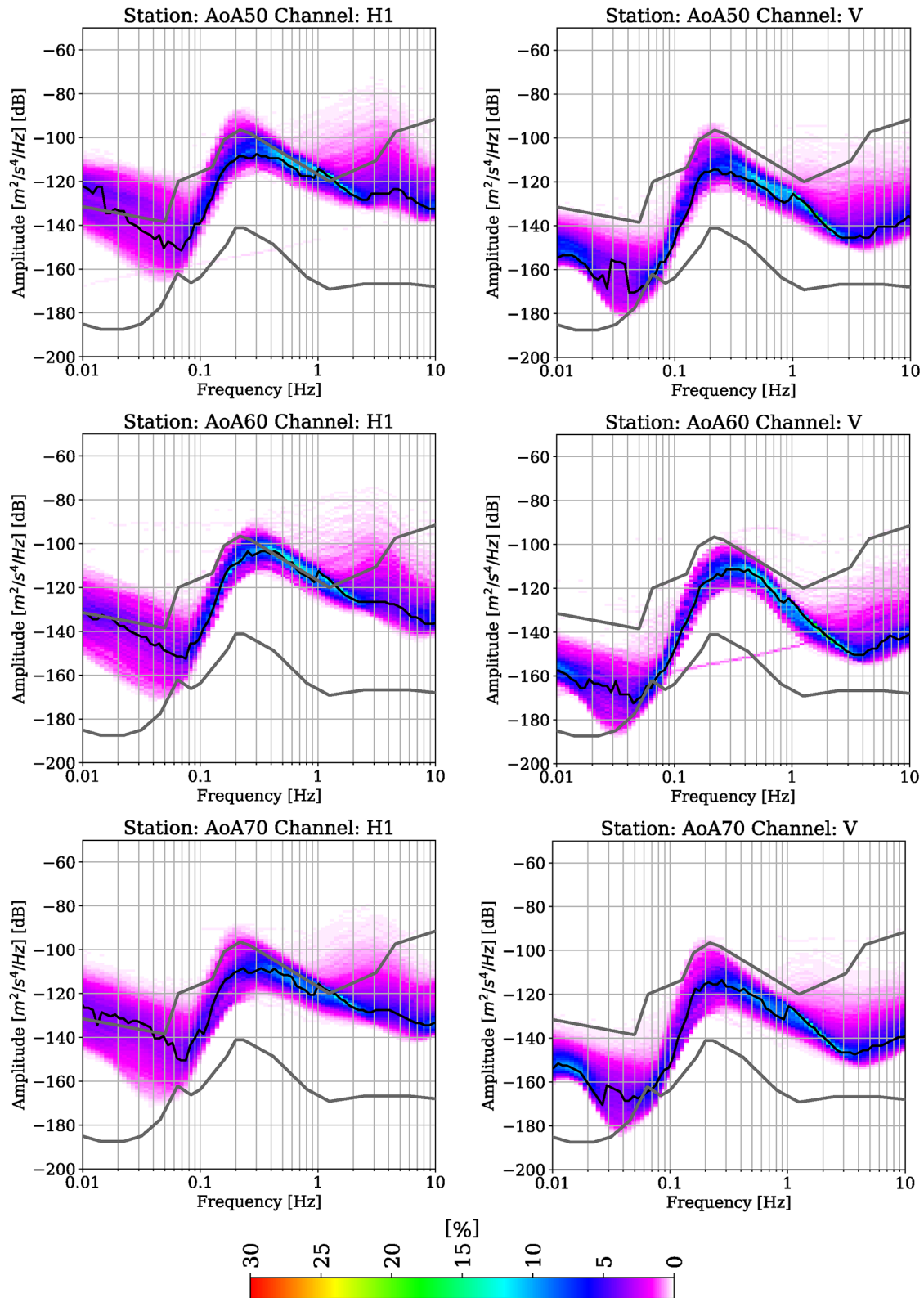
Figure 6. Probabilistic power spectral density (PPSD) of the east (H1) and vertical (V) components for station AoA50 (1st row), AoA60 (2nd row) and AoA70 (3rd row) during the period of 2016 September 25 to 2017 September 15. The thick grey lines at the bottom and top represent the NLNM and NHNM, respectively, from Peterson (1993). The solid black line indicates the energy mode of the SAN level. The colour bar at the bottom depicts the probability of occurrence of a given power at a certain frequency. PPSD plots of the H2 components are presented in Supplementary Fig. S2.

Table 1. The range of layer parameters used for H/V curve inversion at OBS station AoA51. The topmost and the bottom layers represent the water layer and the half-space, respectively.

V_P (m s^{-1}) min–max	V_S (m s^{-1}) min–max	h (m) min–max
1450–1500	0–0	2850–2850
1450–2500	25–200	1.3–2
1450–3000	100–400	4–10
1450–4000	100–1200	20–80
1450–7000	100–4000	30–200
1450–7000	100–4000	650–1200
1450–7000	100–4500	1300–1700
1450–8000	100–5000	2600–2900
1450–8500	100–5000	2100–2900
1450–9000	100–6000	0

the upper 10 km. While setting the initial range of V_S for the uppermost layer (i.e. the surface layer at the seabed), we utilized V_S values from the literature, that is 25 to 90 m s^{-1} (e.g. Huerta-López *et al.* 2003) and considered a very high V_P/V_s ratio (e.g. Hamilton 1979). To set the parameter space for the V_S values of some of the shallow layers within the Tertiary sedimentary sequences, we also considered high V_P/V_s ratios, where the initially considered V_P values were again from drilling data (Shipboard Scientific Party 2000) and Miura *et al.* (2003). The starting velocities (both V_P and V_s) were equal for all of the layers with wide upper bounds, allowing the parameter space to be regarded as non-informative and the inversion algorithm to have sufficient liberty to search for the best representative model for the investigated OBS site. During parametrization, the elastic properties of the water layer (V_P = 1450–1500 m s^{-1}, V_S = 0 m s^{-1}, ρ = 1000 kg m^{-3}) were added along with the thickness of the water column (the elevation of the sensor in relation to the MSL, Fig. 2). Table 1 presents parametrization of one representative station (AoA51) from this study, the inversion result of which is shown in Fig. 7.

4.3.3 Misfit function

The inversion process uses the improved neighbourhood algorithm (Wathelet 2008), which is a direct stochastic search procedure to allow for suitable exploration and exploitation of the parameter space. In this inversion scheme, the parameter space is partitioned into 50 starting models by using the Voronoi cell concept. For each model the misfit is estimated. Next, 50 new models are generated in each iteration and assembled according to the best previous model. This process is iterated a sufficiently large number of times to allow for suitable exploration and exploitation of the parameter space. The misfit function is defined as (Lontsi *et al.* 2015):

$$\text{hvmisfit} = \sqrt{\frac{1}{N}\sum_{i=1}^{N}\frac{\left(\log\left(\frac{H}{V_{m_i}}\right)-\log\left(\frac{H}{V_{d_i}}\right)\right)^2}{\sigma_{d_i}^2}}, \quad (4)$$

where N = total number of frequencies, H/V_d is the observation and H/V_m is assigned to the generated models. The standard deviation of the observation at a certain frequency is denoted by σ_d.

4.3.4 Inversion results

Within the selected maximum misfit range, numerous models were provided in the output after termination of the iterations. One best-fitting model with the smallest misfit was also highlighted as an outcome (Fig. 7 and Supplementary Figs S3, S4 and S5). The best

V_S velocity profile from the H/V curve inversion was considered as the final profile. The obtained minimum misfit value for all stations was below 2.4. The velocities were fairly constrained in spite of the loosely bounded parameter spacing. The V_S profiles from the seabed to 7000 mbsf are shown in Figs 8(a), 9(a) and 10(a). To clearly demonstrate the very shallow sedimentary profiles with high resolution, velocity profiles at a 30 m depth were plotted separately (Figs 8b, 9b and 10b) along with the full profile.

4.4. Assessing the effect of the water layer on the H/V ratio

To investigate the effect of the water layer, we compared the observed H/V curves with those modelled with and without a water layer (Fig. 11 and Supplementary Fig. S6). When removing the water layer from the best inversion model, the synthetic H/V curves of all the stations exhibited a remarkable increase in amplitude around the predominant peak at higher frequencies (1–5 Hz), with variable effects (comparatively little or no increase) observed at lower frequencies (<1 Hz). Notably, no significant shift in the predominant peak was observed between the synthetic and observed models.

After removing the water layer from the model, the stations of AoA5 showed an amplitude increase of 62–98 percent around the predominant peak and 0–8 percent at lower frequencies. Stations of AoA6 showed an amplitude increase of 47–105 percent around the first predominant peak at higher frequencies, 72–109 percent around the second predominant peak and 4–66 percent at the lower frequencies, with an almost 89 percent increase observed at station AoA60. Stations of AoA7 showed an amplitude increase of 58–104 percent around the predominant peak and 0–42 percent at lower frequencies.

5 RESULTS AND DISCUSSION

5.1. Observed H/V curves

In the observed H/V curves (within 0.1 to 10 Hz frequencies), the major peak frequency was within 4–5.1 Hz at AoA5 and AoA7, except for stations AoA70 and AoA75 where it was 3–4 Hz (Fig. 4). Meanwhile, at AoA6, the predominant frequency peak was observed within 3–4 Hz. The predominant peak at higher frequencies may have resulted from the impedance contrast at the interface between the thin water-saturated soft seabed sedimentary layer and a relatively compacted and lithified deeper layer.

Notably, the curves for the AoA6 stations differed slightly from those at the other locations because of having a double-frequency peak-like feature within 1–2 Hz. Note that the AoA5 and AoA7 arrays were offset by ~60 km from the trench axis in the perpendicular direction and landwards to the east, whereas that for AoA6 was ~40 km.

Apart from the major peak, the observed H/V curves for all stations demonstrated four to five minor undulations or small-amplitude peak-like features above an amplitude of 2—they became gentler at lower frequencies (Fig. 4). These changes in amplitude with frequency might reflect changes in wave velocities as well as the layer-to-layer impedance contrast with depth (Piña-Flores *et al.* 2017). Indeed, a decrease in the impedance contrast with depth could cause lower amplitudes in the H/V curves at lower frequencies (Schleicher & Pratt 2021). It is also evident from the *P*-wave results of the previous study (Figs 1b and c) that the velocity contrast varies little from layer to layer, but increases gradually with depth.
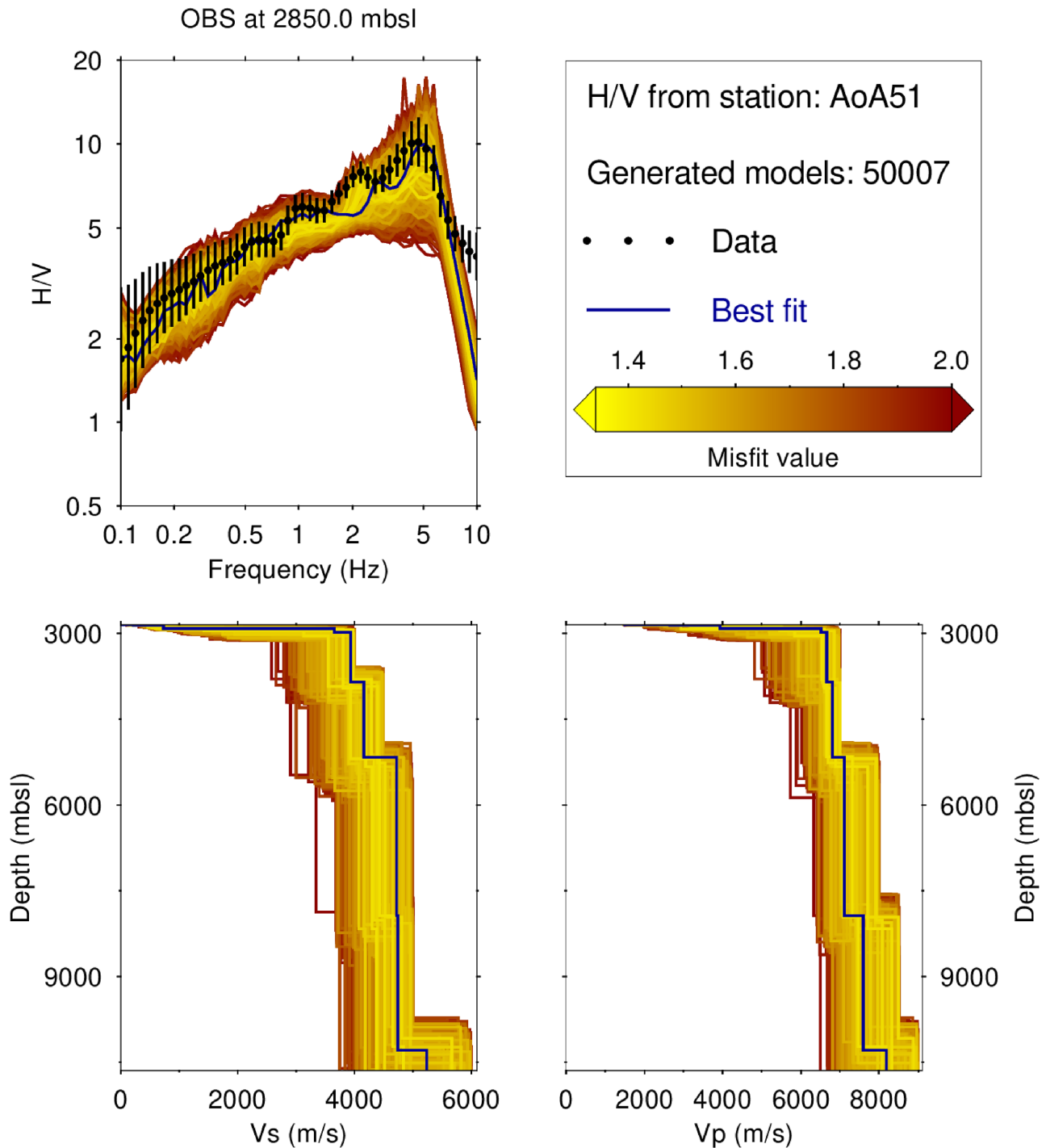
Figure 7. Representative H/V inversion result for station AoA51 with misfit information and synthetic models. The observed and generated H/V curve models are presented in the top left-hand panel; misfit information is presented in the top right-hand panel (only misfits ranging from the lowest to a selected upper value are shown, and only the models associated with them are presented in the other panels); the best-fitting V_S with the generated models is presented in the bottom left-hand panel; and the best-fitting V_P with the generated models is presented in the bottom right-hand panel. Inversion results for the remaining stations are presented in Supplementary Figs S3–S5. mbsl: metre below sea level.

H/V curves between 0.7 and 10 Hz may reflect the major layers within the Tertiary sedimentary sequences. The broad low-amplitude peak-like feature at 0.4–0.6 Hz at all stations could be representative of the demarcation boundary between the Cretaceous and overlying Tertiary sedimentary sequences (Tsuru *et al.* 2002; Miura *et al.* 2003), which was also evident from our forward modelling. The broad nature of this low-amplitude peak-like feature

could represent the low-velocity contrast as well as the complex nature of the subsurface. An even gentler and lower amplitude peak-like feature of the H/V curves at 0.1–0.2 Hz for all stations is considered to reflect the velocity contrast between the island arc upper crust and overlying Cretaceous sedimentary sequences. However, the velocity contrast was not high enough to cause a high-amplitude peak, similar to the previous *P*-wave survey result
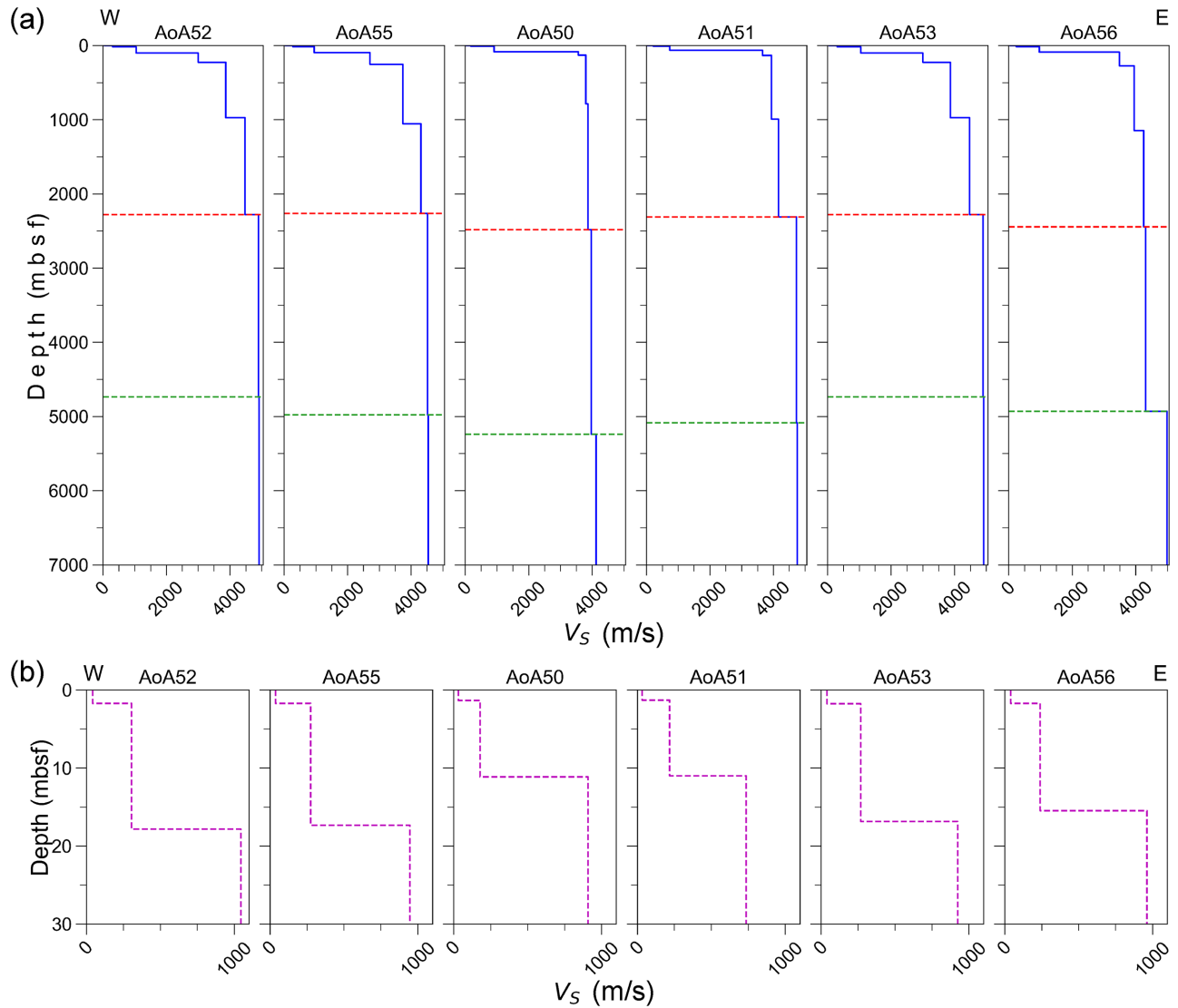
Figure 8. (a) V_S profiles, up to 7000 mbsf, from the OBS stations of array AoA5. The red dotted line represents the unconformity between the Tertiary and the Cretaceous sedimentary sequences. The green dotted line represents the boundary between the Cretaceous sedimentary sequences and the island arc upper crust. (b) Shallow profiles, up to 30 m depth.

(Figs 1b and c). The similarity in the H/V curve below 1 Hz for all stations is considered to reflect the deeper subsurface features at these low frequencies.

5.2. Noise levels in the offshore Fukushima region

The characterization of noise energy compared with the NHNM and NLNM of Peterson (1993), especially at lower frequencies (< 0.1 Hz), could verify the cause of the stable frequency range and elucidate important subsurface information for H/V analysis. Here, we discuss noise power levels according to four well-recognized frequency bands.

(i) *Very low to low frequency band (<0.02 Hz)*

In this frequency band, the noise energy on the vertical (V) component was well within the NHNM and NLNM. In contrast, the noise energy levels for the horizontal components (H1 and H2) fluctuated greatly (∼25 dB), with many PSDs and the noise mode exceeding the NHNM (Fig. 6 and Supplementary Fig. S2). Moreover, an

∼30 dB difference between the noise levels of the horizontal and vertical components was evident from the noise mode. Tilt noise induced by seafloor currents give rise to such unstable and elevated SAN levels in this frequency band—a relatively small tilt by ocean currents could introduce considerable noise in the horizontal component (Webb 1998; Dahm *et al.* 2006; Angelis & Bodin 2012; Nishida 2017).

(ii) *Primary microseism band (0.02–0.1 HZ)*

Noise in this frequency band can be generated by conversion of far-field energy induced by very large oceanic storms, low-frequency ocean wave energy or seismic energy generated by vertical pressure variation of ocean currents at the seafloor or by breaking of surf on a sloping beach (Hasselmann 1963; Webb 1998; McNamara & Buland 2004). Noise power in this band is completely dependent on climatic conditions (Grecu *et al.* 2018). A smearing effect by low probability PSDs on the PPSD was observed below 0.1 Hz due to surface waves from teleseismic arrivals (McNamara and Buland 2004, see Figs 4 and 8).
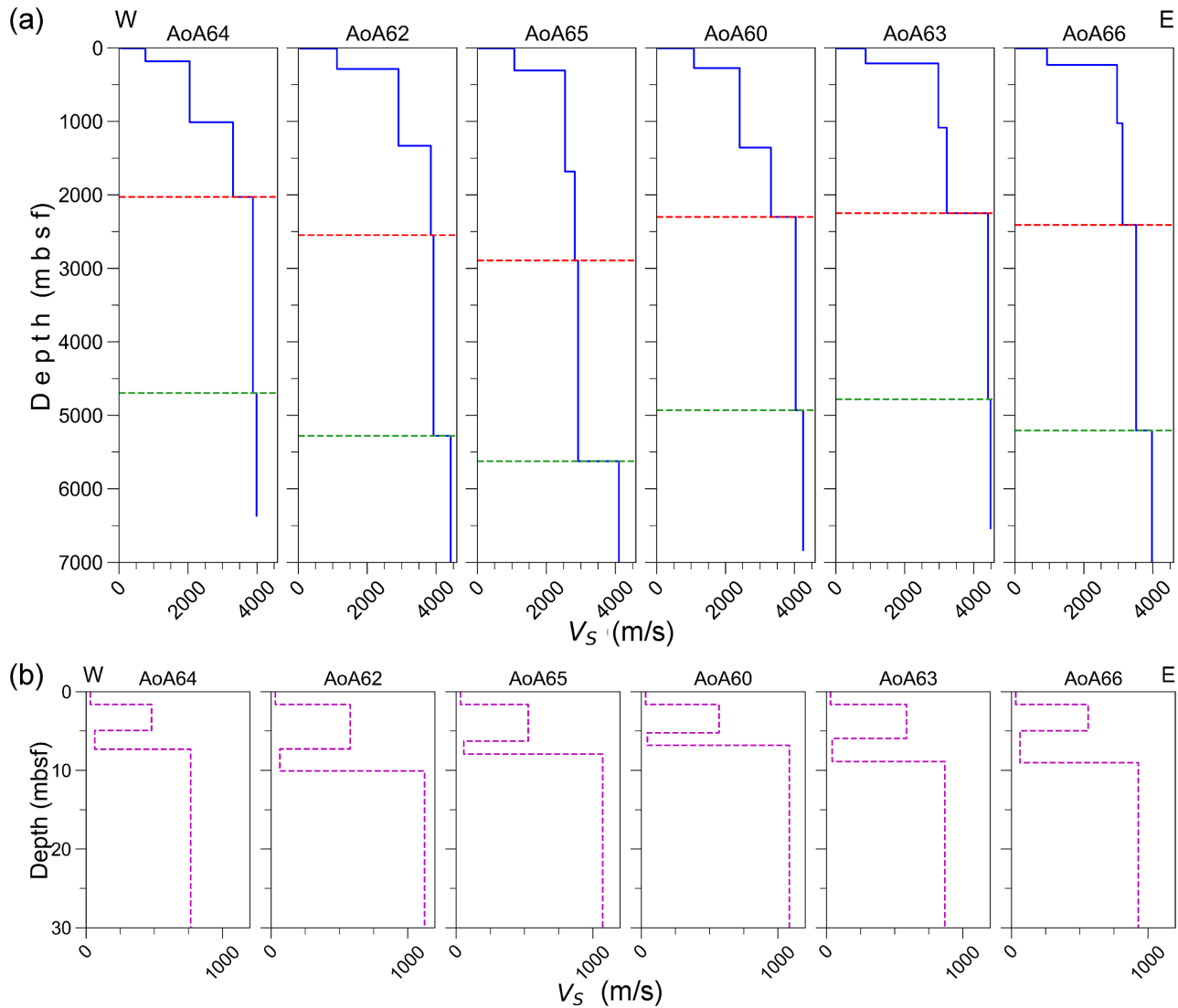
Figure 9. (a) V_S profiles, up to 7000 mbsf, from the OBS stations of array AoA6. The red dotted line represents the unconformity between the Tertiary and the Cretaceous sedimentary sequences. The green dotted line represents the boundary between the Cretaceous sedimentary sequences and the island arc upper crust. (b) Shallow profiles, up to 30 m depth.

Within this frequency band, the energy modes of the horizontal components corresponded with the NLNM and NHNM of Peterson (1993), except those of OBS AoA70, where the noise modes exceeded the NHNM below 0.04 Hz (Fig. 6 and Supplementary Fig. S2). A tiny microseism peak was discernible in the horizontal components. The PSDs in the horizontal components showed energy variations of ∼20 dB. A sharp increasing trend was observed for many PSDs, exceeding the NHNM. A sharp increasing trend was also observed in the noise mode of the horizontal components from ∼0.07 Hz at all stations. Such unstable and elevated SAN energies are related to tilt noise on the horizontal components (Webb 1998; Crawford & Webb 2000; Bell *et al.* 2015).

Within this frequency band, the PSDs as well as the noise mode of the vertical component were within the NHNM and NLNM (Peterson 1993), but with a gentler increasing slope than that of the horizontal component. The noise mode power of the vertical component was ∼20 dB lower than that of the horizontal components. At around 0.03–0.04 Hz there was a broad peak in the vertical component, which might be related to compliance noise caused by the

elastic deformation of earth material below the seismometer owing to pressure variations induced by oceanic gravity waves (Crawford & Webb 2000; Bell *et al.* 2015; Tian & Ritzwoller 2017). However, this compliance noise peak was absent in the vertical component of station AoA60 where the water depth was much greater (Fig. 2). It is known that compliance noise is sensitive to water depth and that oceanic gravity wavelengths have to be greater than the water depth to cause such noise on an OBS (Crawford & Webb 2000; Bell *et al.* 2015; Tian & Ritzwoller 2017).

(iii) *Secondary microseism band (0.1–1 Hz)*

This band was consistently the most energetic part of the PPSD plots within 0.01 to 10 Hz (Fig. 6 and Supplementary Fig. S2). The PSDs with high probability were mostly below the NHNM for all components, including the noise energy mode. The horizontal components in this band were ∼10 dB higher than the vertical components. The origin of the secondary microseism peak is related to standing gravity waves, the amplitude of which could be markedly increased by local storms (Longuet-Higgins 1950; McNamara and
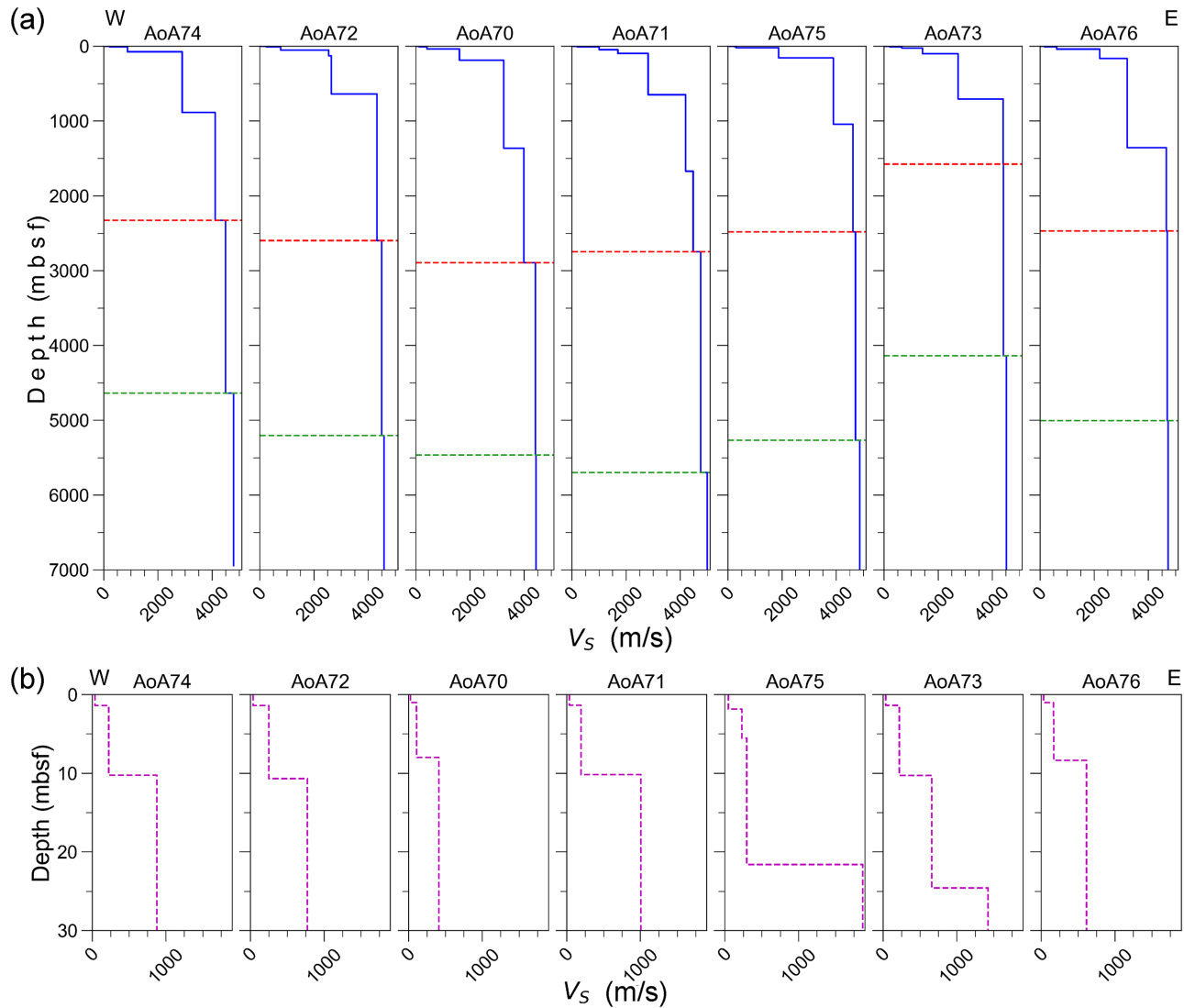
Figure 10. (a) V_S profiles, up to 7000 mbsf, from the OBS stations of array AoA7. The red dotted line represents the unconformity between the Tertiary and the Cretaceous sedimentary sequences. The green dotted line represents the boundary between the Cretaceous sedimentary sequences and the island arc upper crust. (b) Shallow profiles, up to 30 m in depth.

Buland 2004). The secondary microseism peak is not only reported in the global noise model of Peterson (1993) based on observations of land seismic stations worldwide, but in many other areas, both on land and in the ocean (e.g. Webb 1998; McNamara & Buland 2004; Vassallo *et al.* 2012; Nishida 2017; Baker *et al.* 2019).

   (iv) *High frequency noise band (>1 Hz)*:

   In the high-frequency range (>1 Hz), peaks were registered on all horizontal components of all three broad-band stations (Fig. 6 and Supplementary Fig. S2). Webb (1998) reported this peak on the ocean floor (Webb 1998, see Figs 1 and 6), though it is generally related to the wavefield of short-wavelength shear modes, also known as Stoneley or Scholte waves, produced by local winds of short periodic nature. SAN within this range is frequently used on land for H/V computation and shallow subsurface characterization (Nakamura 1989, 2000), where this frequency band is dominated by contributions from human activities.

   Low-probability smeared signals exceeding the NHNM at >1 Hz were probably related to body waves from local small events of $M_W < 1.5$ (McNamara and Buland, 2004; Vassallo *et al.* 2012).

Shear-mode peaks can limit the detection and location of these small events (Vassallo *et al.* 2012) as well as body waves of short-period teleseismic arrivals $m_b = 7.5$ (Webb 1998). Notably, the arrivals of short-period V_P are identifiable only at amplitudes greater than the noise power level (Webb 1998).

5.2.1. Influence of noise energy on the H/V curve

The H/V curves computed from seismic noise within 0.1 to 10 Hz (Fig. 4) were stable for all the OBS stations. However, temporally unstable conditions with unusually large amplitudes were found below 0.1 Hz, as computed using data from the three broad-band OBSs (Fig. 3). At lower frequencies, the ocean is noisier than the land (Crawford & Webb 2000). Hence, our intention here is to discuss the unstable condition of H/V ratios at lower frequencies (<0.1 Hz) based on our PSD analysis (Fig. 5 and Supplementary Fig. S2). To the best of our knowledge, this is the first observation comparing low-frequency (<0.1 Hz) H/V ratios with PSDs at the ocean bottom.
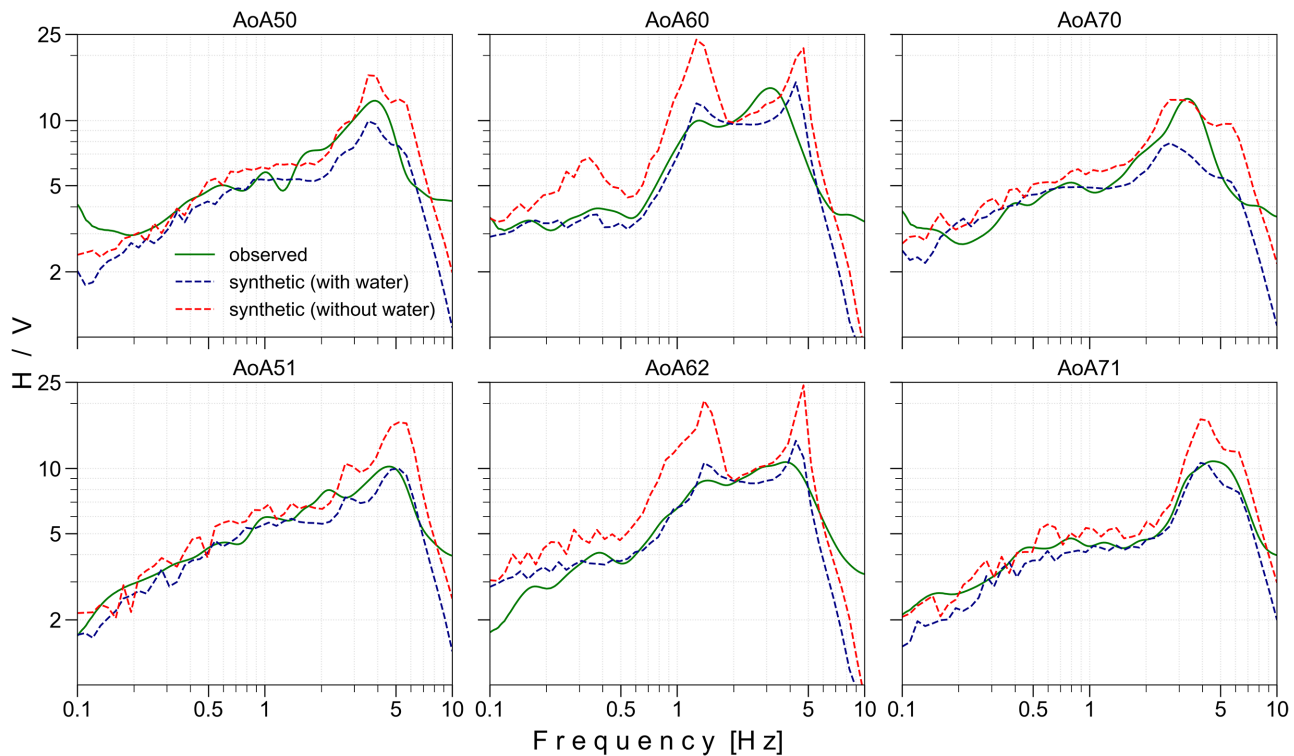
Figure 11. Water layer effect on the H/V curve from six example stations among the three arrays. Synthetic H/V obtained by removing the water layer from the best profile of the inversion model (dashed red line) compared with the H/V curve from the best profile with the water layer (dashed blue line) and the observed H/V curve (solid green line). The water layer effects on the H/V curve of the remaining stations are presented in Supplementary Fig. S6.

It is evident that the SAN energy was stable within 0.1 to 10 Hz and corresponded with the NHNM and NLNM. The temporally unstable H/V ratios below 0.1 Hz (Fig. 3) for all broad-band OBSs could be related to the unstable and elevated SAN energy levels in the horizontal components caused by the tilt noise induced by ocean floor currents (Webb 1998; Crawford & Webb 2000; Dahm *et al.* 2006; Angelis & Bodin 2012; Bell *et al.* 2015). Compliance noise in the vertical component was also observed at two shallower broad-band OBS stations (AoA50 and AoA70), but not at the deeper OBS station (AoA60). In this context, similarly unstable H/V ratios (<0.1 Hz) at all the broad-band OBS stations could indicate that they are related mainly to the tilt noise in the horizontal components. However, the lack of additional OBS data for the deeper ocean (like AoA60) in this study limits the verification of this observation, and thus demanding further research.

5.3. *S*-wave velocity profiles

V_S structures were estimated from the seabed to 7000 mbsf, including the sedimentary layers and the island arc upper crust. The V_S values ranged from ∼30 to ∼4900 m s^{-1} at different layers, increasing with depth (Figs 8–10). In the loose soft water-saturated sediments at the surface of the seabed, V_S has been frequently reported to range from 25 to 90 m s^{-1} (Webb 1998; Huerta-López *et al.* 2003; Shynkarenko *et al.* 2021). After this very thin (1.3 to 1.8 m) layer, the V_S value was approximately 200 m s^{-1} at the top to approximately 4400 m s^{-1} at the bottom of the Tertiary sedimentary sequences. The top several-hundred meters (∼600 m) are considered to be Quaternary sequences (Chester *et al.* 2013a), with V_S values ranging from 200 to 2000 m s^{-1}. However, the total thickness of the Tertiary sedimentary sequences obtained in our study

was approximately 2100–2600 m, with an unconformity reported between these sequences and the underlying Cretaceous sedimentary sequences, similar to the results of Miura *et al.* (2003, ∼2000 to 3000 m). To explain the lower frequency peak (within 1 to 2 Hz) among the double frequency peaks of the AoA6 stations, a very thin (1.6 to 4.055 m) and low-velocity layer (V_S values from 43 to 64 m s^{-1}) had to be introduced before the layer related to this peak. The depth of this low-velocity layer was approximately 5–6 mbsf. The V_S value within the Cretaceous sedimentary sequences ranged from 3883 to 4600 m s^{-1}, with the observed thickness varying from approximately 2392 to 2951 m; this value was reported to be around 2800 m by Miura *et al.* (2003). The velocity in the island arc upper crust was approximately 3971–4900 m s^{-1}; the thickness of this layer could not be determined in this study.

Huang *et al.* (2011) presented the V_S structure 50 km north of our study area using anisotropic tomography, with initial model from Zhao *et al.* (1992), and found that the average velocity in the upper crust was a maximum of ∼3800 m s^{-1}. It should be noted that their results were of a relatively low resolution in the offshore compared to the onshore region, especially for depths less than 10 km. Liu & Zhao (2016) also presented V_S velocity information in the study area using local and teleseismic earthquake and surface wave tomography, with no resolution in the upper 10 km of the subsurface but only an average velocity. Fig. 12 exhibits a comparison of the V_S profiles from this study with previous studies conducted in and around the study area. The V_P profiles are also presented with the background earth structure to provide a better understanding of the velocity changes in the subsurface. Compared to previous studies, the inverted V_S with depth tended to be higher in many cases. This is because individual layers were considered rather than a single value over the entire upper crust. In this context, the consequences
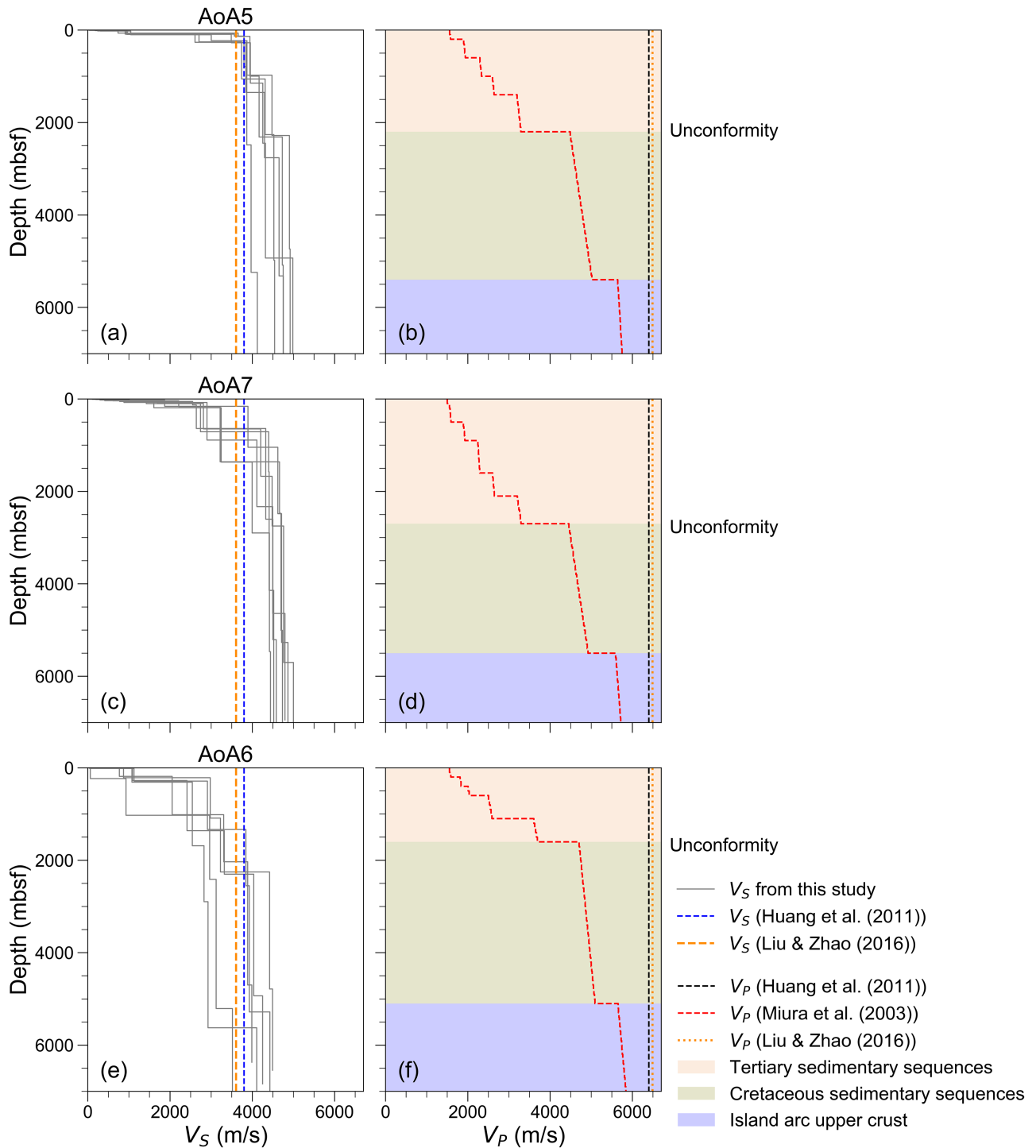
Figure 12. The inverted V_S profiles are presented here with the V_S and V_P profiles from previous studies. (a, c, e) V_S profiles of the arrays AoA5, AoA7 and AoA6, respectively; (b, d, f) V_P profiles from previous studies, with the background earth structure from Miura *et al.* (2003). (b) represents the V_P profile from a nearby point of line FK201 of Miura *et al.* (2003); (d, f) represent V_P profiles from a nearby point of line FK102; in each case, the water depth in the selected profile was similar to that of the OBS array.

of using a wide initial parameter space and the effect of the trade-off between velocity and depth could not be disregarded. Notably, as the study area is very close to an active oceanic subduction zone, sediments in this region are overcompacted and are often composed of volcanic materials from the Japan Arc (Shipboard Scientific Party 2000) to result in higher V_S values with depth.

The very shallow profiles (up to 30 m) of each OBS array are plotted in Fig. 13 along with the V_P profiles extracted from two sites (site 438 and 440) of the Ocean Drilling Program at the Japan Trench off northeast Japan (Shipboard Scientific Party 2000) and from Miura *et al.* (2003). To our knowledge, no V_S profile with similar sensitivity for shallow depths is available for this region to allow for a
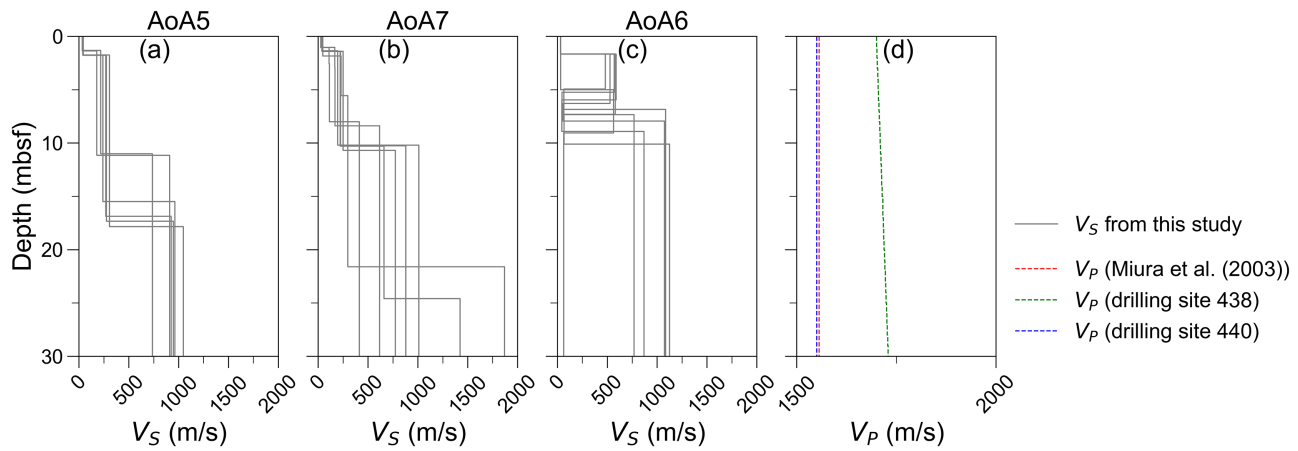
Figure 13. The inverted V_S profiles up to a 30 m depth are shown here with the V_P profiles that were sensitive to shallow depth from previous studies. (a, b, c) V_S profiles of the arrays AoA5, AoA7 and AoA6, respectively; (d) V_P profiles from previous studies, V_P profiles from two sites of the Shipboard Scientific Party (2000) are referred to in the figure as 'drilling site 438' and 'drilling site 440'. Drilling site 440 may be referred to arrays AoA5 and AoA7, as this site is in the updip portion of the subducting crust and has water depths closer to those in the array sites. Drilling site 438 may be referred to array AoA6, as this site is in the downdip portion of the subducting crust and has water depths closer to those for AoA6. V_P velocity from Miura *et al.* (2003) is similar for the upper 100 m in all sites; therefore, only one such profile is presented in (d). No comparable V_S profile for shallow depths is available in this region.

comparison with the present results. Nonetheless, Fig. 13 helps to discern a very high V_P/V_S ratios of oceanic sediments at shallow depths (Hamilton 1979).

Although the solution of the H/V spectral ratio inversion alone may suffer from non-uniqueness and trade-off between the shear wave velocity and layer thickness, the constraints introduced using prior information allow us to consider the presented velocity profiles as the most representative profiles of the seismic structure at the investigated OBS sites at this time. However, the profiles may be updated in the future as new data for the depths of interest, such as dispersion curves, geotechnical data or H/V from boreholes, etc., become available for the study area. While no other studies in the offshore Fukushima region have focused on V_S velocity structures within the sedimentary and igneous island arc upper crust layer, the high-resolution shallow velocity profiles presented in this study could benefit future seismological studies, including those on receiver function analysis, tomography and earthquake detection, as a preliminary guideline. This study provides empirical support for the noise-based full H/V spectral ratio curve inversion technique considering full waveforms (based on the DFA) to determine high-resolution V_S velocity information down to <10 km of the subsurface in an oceanic environment.

5.4. Effect of the water layer on the H/V curve

The synthetic H/V analysis considered the lower frequency range up to 0.1 Hz and the subsurface of 7000 mbsf, where the maximum thickness of the water layer was ∼4280 m. Lontsi *et al.* (2019) considered the lower frequency range up to 0.2 Hz and the subsurface of 102.9 mbsf with a maximum water layer thickness of 5000 m, with a different subsurface setting from this study. They reported significant changes in the amplitude around the major peak of the observed curve near 1 Hz with only a marginal peak shift when the water layer was removed. Moreover, Lontsi *et al.* (2019) considered onshore data, where water layers of various thickness were synthetically introduced to demonstrate the response of the H/V curve to water layers. In contrast, this study explicitly considers offshore data to investigate such effect on the H/V ratios. However, the effect of subsurface layering complicates the models, so it is important to

estimate the effect of the water layer on the H/V curve using forward modelling at various sites with different subsurface conditions.

In this study, a similar result like Lontsi *et al.* (2019), with respect to the amplitude variation, was found around the higher frequency (>1 Hz) predominant peak amplitude, which varied between 47 percent and 109 percent among the stations. Interestingly, significant peak amplitude variation was found for both of the double frequency peaks of the H/V curves for AoA6. However, like the results of Lontsi *et al.* (2019), the rest of the curve amplitude in the lower frequencies exhibited various effects for different stations, such as no (approximately 0 percent) to very little and some significant (around 4 to 89 percent) increases when the water column was removed (Fig. 11 and Supplementary Fig. S6).

From the synthetic test, it is evident that the overlying water layer has a constant predominant effect within the higher frequency (>1 Hz) portion of the H/V curve, whereas it is substantially smaller and variable at lower frequencies (<1 Hz). Lontsi *et al.* (2019) showed by DED modelling that the horizontal components of an OBS are unaffected by the water column, while a large *P*-wave energy on the vertical component, due to multiple reverberations in the water column, causes amplitude variation on the H/V curve. Various amplitude variation in the lower frequencies (<1 Hz) caused by various resonances could be related to water layer thickness as well as complex subsurface structures; these factors require further scrutiny.

6 CONCLUSIONS

H/V curves for the frequency ranges of 0.01 to 10 Hz and 0.1 to 10 Hz were derived, from three broad-band and sixteen short-period OBSs, respectively, in the Fukushima forearc region of the southern Japan Trench area. We found that the H/V ratios between 0.1 and 10 Hz were stable, whereas ratios below 0.1 Hz were unstable and, therefore, could not be used to retrieve subsurface information. High temporal variability and elevated SAN energy was found at the lower frequencies (<0.1 Hz) due to tilt and compliance noise, with the horizontal components in particular being highly contaminated. This analysis helps us understanding why the H/V curves below 0.1 Hz are large and unstable, and may have some bearing upon

future deployment procedures. Using H/V analysis, subsurface V_S profile estimation and subsequent delineation of the major geological structures were performed down to 7000 mbsf in the offshore Fukushima region. The obtained V_S structures roughly agreed with the available geological information at the study area. The seismic velocity at the surface layer was ~ 30 m s^{-1} and increased from 200 to 4400 m s^{-1} within the tertiary sedimentary sequences. Furthermore, the unconformity between the Tertiary and Cretaceous sedimentary sequences was successfully identified, which was consistent with the results of previous studies (at approximately 2100–2600 mbsf). The velocity within the Cretaceous unit ranged from 3883 to 4600 m s^{-1}, and that in the island arc crust ranged from 3971 to 4900 m s^{-1}. This is the first observation leading to high-resolution information within the sedimentary layers and island arc upper crust for offshore Fukushima. Therefore, the presented velocity profiles may be utilized as preliminary guidelines for future studies and should be updated when new supporting data become available. Moreover, an investigation of the water layer effect on the H/V curve showed that its inclusion leads to significant amplitude variation around the fundamental peaks within the higher frequencies (> 1 Hz), while less variation was observed at lower frequencies (0.1 to 1 Hz); this result might be related to the water layer thickness and complex subsurface structure, though these factors require further scrutiny.

The Japan Trench has potential for active seismicity and very large seismic events (e.g. the 2011 Tohoku earthquake, M_W 9). We believe that the noise energy levels and V_S information provided in this study could increase the accuracy of slow earthquake detection studies and subsurface imaging in the Japan Trench region with assorted seismic methods.

Author Contributions: AHF performed all data processing and analyses while contributing to the writing of the manuscript. YI supervised the study. ESMG contributed to coding and writing of the manuscript. AML, FJSS and AJ developed and tested the code for full H/V inversion and used 'hvgeneralized' in the forward modelling ('hvgeneralized'). AJ aided in the implementation of 'hvgeneralized' in the coding environment. SO, RH and MS were

responsible for OBS deployment and maintenance as well as data collection.

DATA AVAILABILITY

The OBS data used in this study cannot be shared publicly, as determined by the stakeholders.

Conflict of Interest

The authors declare that they have no known competing financial interests or personal relationships that could have appeared to influence the work reported in this paper.

REFERENCES

Aki, K., 1957. Space and time spectra of stationary stochastic waves, with special reference to microtremors, *Bull. Earthq. Res. Inst.,* **35,** 415–456. Available at: https://ci.nii.ac.jp/naid/10003122622

Altamimi, Z., Collilieux, X., Legrand, J., Garayt, B. & Boucher, C., 2007. ITRF2005: a new release of the International Terrestrial Reference Frame based on time series of station positions and Earth Orientation Parameters, *J. geophys. Res. Solid Earth,* **112,** 9401, doi: 10.1029/2007JB004949

Angelis, S. & Bodin, P., 2012. Watching the Wind: seismic data contamination at long periods due to atmospheric pressure-field-induced tilting, *Bull. seism. Soc. Am.,* **102,** 1255–1265.

Apel, E.V., Bürgmann, R., Steblov, G., Vasilenko, N., King, R. & Prytkov, A., 2006. Independent active microplate tectonics of northeast Asia from GPS velocities and block modeling, *Geophys. Res. Lett.,* **33,** doi: 10.1029/2006GL026077

Arai, H. & Tokimatsu, K., 2004. S-wave velocity profiling by inversion of microtremor H/V spectrum, *Bull. seism. Soc. Am.,* **94,** 53–63.

Ardhuin, F., Gualtieri, L. & Stutzmann, E., 2015. How ocean waves rock the Earth: two mechanisms explain microseisms with periods 3 to 300 s, *Geophys. Res. Lett.,* **42,** 765–772.

Ardhuin, F., Stutzmann, E., Schimmel, M. & Mangeney, A., 2011. Ocean wave sources of seismic noise, *J. geophys. Res. Ocean.,* **116,** doi: 10.1029/2011JC006952

Asten, M. & Boore, D., 2005. Comparison of shear-velocity profiles of unconsolidated sediments near the coyote borehole (CCOC) measured with fourteen invasive and non-invasive methods editorial, *J. Environ. Eng. Geophys.,* **10,** 85–85.

Asten, M.W., Askan, A., Ekincioglu, E.E., Sisman, F.N. & Ugurhan, B., 2014. Site characterisation in north-western Turkey based on SPAC and HVSR analysis of microtremor noise, *Explor. Geophys.,* **45,** 74–85.

Ba, Z., Sang, Q., Liang, J. & Wu, M., 2021. HVSR analysis of a layered saturated Half-space using Diffuse-Field theory, *Geophys. J. Int.,* **226,** 270–286.

Baker, M.G. *et al.*, 2019. Seasonal and spatial variations in the ocean-coupled ambient wavefield of the Ross Ice Shelf, *J. Glaciol.,* **65,** 912–925.

Bao, F., Li, Z., Yuen, D.A., Zhao, J., Ren, J., Tian, B. & Meng, Q., 2018. Shallow structure of the Tangshan fault zone unveiled by dense seismic array and horizontal-to-vertical spectral ratio method, *Phys. Earth planet. Inter.,* **281,** 46–54.

Bard, P.Y. *et al.*, 2010. From non-invasive site characterization to site amplification: recent advances in the use of ambient vibration measurements, *Geotech. Geol. Earthq. Eng.,* **17,** 105–123.

Beauduin, R., Lognonné, P., Montagner, J.P., Cacho, S., Karczewski, J.F. & Morand, M., 1996. The effects of the atmospheric pressure changes on seismic signals or how to improve the quality of a station, *Bull. seism. Soc. Am.,* **86,** 1760–1769.

Bell, S.W., Forsyth, D.W. & Ruan, Y., 2015. Removing noise from the vertical component records of ocean-bottom seismometers: results from year one of the cascadia initiative, *Bull. seism. Soc. Am.,* **105,** 300–313.

Bensen, G.D. *et al.*, 2007. Processing seismic ambient noise data to obtain reliable broad-band surface wave dispersion measurements, *Geophys. J. Int.,* **169,** 1239–1260.

Beyreuther, M., Barsch, R., Krischer, L., Megies, T., Behr, Y. & Wassermann, J., 2010. ObsPy: a Python toolbox for seismology, *Seismol. Res. Lett.,* **81,** 530–533.

Bonnefoy-Claudet, S., Cornou, C., Bard, P.Y., Cotton, F., Moczo, P., Kristek, J. & Fäh, D., 2006b. H,/V ratio: a tool for site effects evaluation. Results from 1-D noise simulations. *Geophys. J. Int.,* **167,** 827–837.

Bonnefoy-Claudet, S., Cotton, F. & Bard, P.Y., 2006a. The nature of noise wavefield and its applications for site effects studies. A literature review, *Earth Sci.Rev.*, **79,** 205–227.

Bora, N., Biswas, R. & Malischewsky, P., 2020. Imaging subsurface structure of an urban area based on diffuse-field theory concept using seismic ambient noise, *Pure appl. Geophys.,* **177,** 4733–4753.

Chester, F.M., Mori, J.J., Eguchi, N. & Toczko, S., Expedition 343/343T Scientists, 2013a. Proceedings of the Integrated Ocean Drilling Program 343/343T Integrated Ocean Drilling Program Management International, *Inc. Tokyo*.

Crawford, W.C. & Webb, S.C., 2000. Identifying and removing tilt noise from low-frequency (<0.1 Hz) seafloor vertical seismic data, *Bull. seism. Soc. Am.,* **90,** 952–963.

Dahm, T., Tilmann, F. & Morgan, J.P., 2006. Seismic Broadband Ocean-Bottom Data and Noise Observed with Free-Fall Stations: experiences from Long-Term Deployments in the North Atlantic and the Tyrrhenian Sea, *Bull. seism. Soc. Am.,* **96,** 647–664.

Dolenc, D., Romanowicz, B., Uhrhammer, R., McGill, P., Neuhauser, D. & Stakes, D., 2007. Identifying and removing noise from the Monterey ocean bottom broadband seismic station (MOBB) data, *Geochem. Geophys. Geosyst.,* **8**. doi: 10.1029/2006GC001403

Fäh, D., Kind, F. & Giardini, D., 2001. A theoretical investigation of average HIV ratios, *Geophys. J. Int.,* **145,** 535–549.

Fäh, Donat, Kind, F. & Giardini, D., 2003. Inversion of local S-wave velocity structures from average H/V ratios, and their use for the estimation of site-effects, *J. Seismol.,* **7,** 449–467.

Farazi, A.H., Hossain, M.S., Ito, Y., Piña-Flores, J., Kamal, A.S.M.M. & Rahman, M.Z., 2023. Shear wave velocity estimation in the Bengal Basin, Bangladesh by HVSR analysis: implications for engineering bedrock depth, *J. Appl. Geophys.,* in revision.

García-Jerez, A., Piña-Flores, J., Sánchez-Sesma, F.J., Luzón, F. & Perton, M., 2016. A computer code for forward calculation and inversion of the H/V spectral ratio under the diffuse field assumption, *Comput. Geosci.,* **97,** 67–78.

Grecu, B., Neagoe, C., Tataru, D., Borleanu, F. & Zaharia, B., 2018. Analysis of seismic noise in the Romanian-Bulgarian cross-border region, *J. Seismol.,* **22,** 1275–1292.

Hamilton, E.L., 1979. V p /V s and Poisson's ratios in marine sediments and rocks, *J. acoust. Soc. Am.,* **66,** 1093–1101.

Hannemann, K. *et al.*, 2014. Three-dimensional shallow structure from high-frequency ambient noise tomography: new results for the Mygdonia basin-Euroseistest area, northern Greece, *J. geophys. Res. Solid Earth,* **119,** 4979–4999.

Haskell, N.A., 1953. The dispersion of surface waves on multilayered media, *Bull. seism. Soc. Am.,* **43,** 17–34. Available at: https://pubs.geoscienceworld.org/ssa/bssa/article-abstract/43/1/17/115661/The-dispersion-of-surface-waves-on-multilayered?redirectedFrom=fulltext

Hasselmann, K., 1963. A statistical analysis of the generation of microseisms, *Rev. Geophys.,* **1,** 177–210.https://doi.org/10.1029/RG001i002p00177

Hellel, M., Oubaiche, E.H., Chatelain, J.L., MacHane, D., Bensalem, R., Guillier, B. & Cheikhlounis, G., 2012. Basement mapping with single-station and array ambient vibration data: delineating faults under Boumerdes City, Algeria, *Seismol. Res. Lett.,* **83,** 798–805.

Horike, M., 1985. Inversion of phase velocity of long-period microtremors to the *S*-wave-velocity structure down to the basement in urbanized areas, *J. Phys. Earth,* **33,** 59–96.

Hua, Y., Zhao, D., Toyokuni, G. & Xu, Y., 2020. Tomography of the source zone of the great 2011 Tohoku earthquake, *Nature Communications,* **11**(1), 1–7.

Huang, Z., Zhao, D. & Wang, L., 2011. Seismic heterogeneity and anisotropy of the Honshu arc from the Japan Trench to the Japan Sea, *Geophys. J. Int.,* **184,** 1428–1444.

Huerta-Lopez, C., Pulliam, J. & Nakamura, Y., 2003. *In situ* evaluation of shear-wave velocities in seafloor sediments with a broadband ocean-bottom seismograph, *Bull. seism. Soc. Am.,* **93,** 139–151.

JAMSTEC 1998. KAIREI CRUISE (KR98-04) Seismic Survey off Fukushima-Miyagi,*Cruise reports,* Tsuru, Tetsuro, 1–52, Japan Marine Science and Technology Center, Yokosuka, Kanagawa, Japan, https://www.godac.jamstec.go.jp/cr_catalog/view/metadata?key=KR98-04_all&lang=en.

Konno, K. & Ohmachi, T., 1998. Ground-motion characteristics estimated from spectral ratio between horizontal and vertical components of microtremor, *Bull. seism. Soc. Am.,* **88,** 228–241.

Kugler, S., Bohlen, T., Forbriger, T., Bussat, S. & Klein, G., 2007. Scholte-wave tomography for shallow-water marine sediments, *Geophys. J. Int.,* **168,** 551–570.

Lacoss, R.T., Kelly, E.J. & Toksöz, M.N., 1969. Estimation of seismic noise structure using arrays, *Geophysics,* **34,** 21–38.

Lecocq, T. *et al.*, 2020. Global quieting of high-frequency seismic noise due to COVID-19 pandemic lockdown measures, *Science,* **369,** 1338–1343.

Lermo, J. & Chávez-García, F.J., 1993. Site effect evaluation using spectral ratios with only one station, *Bull. seism. Soc. Am.,* **83,** 1574–1594.

Liu, X. & Zhao, D., 2016. *P*- and *S*-wave tomography of Japan subduction zone from joint inversions of local and teleseismic travel times and surface-wave data, *Phys. Earth planet. Inter.,* **252,** 1–22.

Longuet-Higgins, M.S., 1950. A theory of the origin of microseisms, *Philos. Trans. R. Soc. London. Ser. A, Math. Phys. Sci.,* **243,** 1–35.

Lontsi, A.M. *et al.*, 2019. A generalized theory for full microtremor horizontal-to-vertical [H/V(z, f)] spectral ratio interpretation in offshore and onshore environments, *Geophys. J. Int.,* **218,** 1276–1297.

Lontsi, A.M., Ohrnberger, M., Krüger, F. & Sánchez-Sesma, F.J., 2016. Combining surface-wave phase-velocity dispersion curves and full microtremor horizontal-to-vertical spectral ratio for subsurface sedimentary site characterization, *Interpretation,* **4,** SQ41–SQ49.

Lontsi, A.M., Sánchez-Sesma, F.J., Molina-Villegas, J.C., Ohrnberger, M. & Krüger, F., 2015. Full microtremor H/V(z,f) inversion for shallow sub-surface characterization, *Geophys. J. Int.,* **202,** 298–312.

Manea, E.F., Cioflan, C.O., Coman, A., Michel, C., Poggi, V. & Fäh, D., 2020. Estimating geophysical bedrock depth using single station analysis and geophysical data in the extra-carpathian area of Romania, *Pure appl. Geophys.,* **177,** 4829–4844.

Maranò, S., Reller, C., Loeliger, H.A. & Fäh, D., 2012. Seismic waves estimation and wavefield decomposition: application to ambient vibrations, *Geophys. J. Int.,* **191,** 175–188.

McNamara, D.E. & Buland, R.P., 2004. Ambient Noise Levels in the Continental United States, *Bull. seism. Soc. Am.,* **94,** 1517–1527.

Miura, S., Kodaira, S., Nakanishi, A., Tsuru, T., Takahashi, N.N., Hirata, N. & Kaneda, Y., 2003. Structural characteristics controlling the seiscicity of the southern Japan Trench fore-arc region, revealed by ocean bottom seismographic data, *Tectonophysics,* **363,** 79–102.

Molnar, S. *et al.*, 2022. A review of the microtremor horizontal-to-vertical spectral ratio (MHVSR) method, *J. Seismol.,* **3,** 1–33.

Muyzert, E., 2007. Seabed property estimation from ambient-noise recordings: part 2—Scholte-wave spectral-ratio inversion, *Geophysics,* **72,** U47–U53.

Nakamura, Y., 1989. A method for dynamic characteristics estimation of subsurface using microtremor on the ground surface, *Railw. Tech. Res. Inst. Q. Rep.,* **30,** 25–33. Available at: https://trid.trb.org/view/294184

Nakamura, Y., 2000. Clear identification of fundamental idea of Nakamura's technique and its applications, Spectrum, in *12th World Conf. Earthq. Eng., Auckland, New Zealand,* 2656. pp. New Zealand Society for Earthquake Engineering. Available at: http://www.sdr.co.jp/papers/n_tech_and_application.pdf

Nakamura, Y., 2008. On the H/V spectrum, in *14th World Conf. Earthq. Eng. October 12-17, 2008, Beijing, China,* pp. 1–10. WCEE. Available at: http://117.120.50.114/papers/14wcee/14wcee_hv.pdf

Nakata, N., Gualtieri, L. & Fichtner, A.(eds.)., 2019. *Seismic Ambient Noise,* Cambridge Univ. Press.

Nishida, K., 2017. Ambient seismic wave field, *Proc. Japan Acad. Ser. B Phys. Biol. Sci.,* **93,** 423–448.

Nishikawa, T., Matsuzawa, T., Ohta, K., Uchida, N., Nishimura, T. & Ide, S., 2019. The slow earthquake spectrum in the Japan Trench illuminated by the S-net seafloor observatories, *Science,* **365**(6455), 808–813.

Nogoshi, M. & Igarashi, T., 1971. On the amplitude characteristics of microtremor (Part 2), *Zisin (Journal Seismol. Soc. Japan. 2nd ser.),* **24,** 26–40.

Ohta, K., Ito, Y., Hino, R., Ohyanagi, S., Matsuzawa, T., Shiobara, H. & Shinohara, M., 2019. Tremor and inferred slow slip associated with afterslip of the 2011 Tohoku earthquake, *Geophys. Res. Lett.,* **46,** 4591–4598.

Overduin, P.P., Haberland, C., Ryberg, T., Kneier, F., Jacobi, T., Grigoriev, M.N. & Ohrnberger, M., 2015. Submarine permafrost depth from ambient seismic noise, *Geophys. Res. Lett.,* **42,** 7581–7588.

Party, S.S., 2000. Proceedings of the Ocean Drilling Program, 186 Initial Reports, *Proc. Ocean Drill. Program, 186 Initial Reports,* Ocean Drilling Program.

Perton, M., Sánchez-Sesma, F.J., Rodríguez-Castellanos, A., Campillo, M. & Weaver, R.L., 2009. Two perspectives on equipartition in diffuse elastic fields in three dimensions, *J. acoust. Soc. Am.,* **126,** 1125–1130.

Perton, Mathieu, Spica, Z.J., Clayton, R.W. & Beroza, G.C., 2020. Shear wave structure of a transect of the Los Angeles basin from multimode surface waves and H/V spectral ratio analysis, *Geophys. J. Int.,* **220,** 415–427.

Peterson, J., 1993. Observations and modeling of seismic background noise, *Open File Rep,* Albuquerque Seismological Laboratory - USGS, 93-322, doi: 10.3133/ofr93322

Picozzi, M., Parolai, S. & Richwalski, S.M., 2005. Joint inversion of H/V ratios and dispersion curves from seismic noise: estimating the *S*-wave velocity of bedrock, *Geophys. Res. Lett.,* **32,** 1–4.

Pilz, M., Parolai, S., Picozzi, M., Wang, R., Leyton, F., Campos, J. & Zschau, J., 2010. Shear wave velocity model of the Santiago de Chile basin derived from ambient noise measurements: a comparison of proxies for seismic site conditions and amplification, *Geophys. J. Int.,* **182,** 355–367.

Piña-Flores, J., Perton, M., García-Jerez, A., Carmona, E., Luzón, F., Molina-Villegas, J.C. & Sánchez-Sesma, F.J., 2017. The inversion of spectral ratio H/V in a layered system using the diffuse field assumption (DFA), *Geophys. J. Int.,* **208,** 577–588.

Poggi, V. & Fäh, D., 2010. Estimating Rayleigh wave particle motion from three-component array analysis of ambient vibrations, *Geophys. J. Int.,* **180,** 251–267.

Qadri, Talha, S.M., Nawaz, B., Sajjad & Sheikh, R.A., 2015. Ambient noise H/V spectral ratio in site effects estimation in Fateh jang area, Pakistan, *Earthq. Sci.,* **28,** 87–95.

Rahman, M.Z., Hossain, M.S., Kamal, A.S.M.M., Siddiqua, S., Mustahid, F. & Farazi, A.H., 2018. Seismic site characterization for Moulvibazar town, Bangladesh, *Bull. Eng. Geol. Environ.,* **77,** 1451–1471.

Rahman, M.Z., Siddiqua, S. & Kamal, A.S.M.M., 2021. Site response analysis for deep and soft sedimentary deposits of Dhaka City, Bangladesh, *Nat. Hazards,* **106,** 2279–2305.

Raspet, R., Hickey, C.J. & Koirala, B., 2022. Corrected tilt calculation for atmospheric pressure-induced seismic noise, *Appl. Sci.,* **12,** 1247, doi: 10.3390/app12031247

Ruan, Y., Forsyth, D.W. & Bell, S.W., 2014. Marine sediment shear velocity structure from the ratio of displacement to pressure of Rayleigh waves at seafloor, *J. geophys. Res. Solid Earth,* **119,** 6357–6371.

Sánchez-Sesma, F.J. *et al.*, 2011. A theory for microtremor H/V spectral ratio: application for a layered medium, *Geophys. J. Int.,* **186,** 221–225.

Sánchez-Sesma, F.J., 2017. Modeling and inversion of the microtremor H/V spectral ratio: physical basis behind the diffuse field approach, *Earth Planets Space,* **69,** 92, doi: 10.1186/s40623-017-0667-6

Sánchez-Sesma, F.J., Pérez-Ruiz, J.A., Luzón, F., Campillo, M. & Rodríguez-Castellanos, A., 2008. Diffuse fields in dynamic elasticity, *Wave Motion,* **45,** 641–654.

Schleicher, L.S. & Pratt, T.L., 2021. Characterizing fundamental resonance peaks on flat-lying sediments using multiple spectral ratio methods: an example from the Atlantic Coastal Plain, Eastern United States, *Bull. seism. Soc. Am.,* **111,** 1824–1848.

Shapiro, N.M., Campillo, M., Stehly, L. & Ritzwoller, M.H., 2005. High-resolution surface-wave tomography from ambient seismic noise, *Science,* **307,** 1615–1618.

Shynkarenko, A., Lontsi, A.M., Kremer, K., Bergamo, P., Hobiger, M., Hallo, M. & Fäh, D., 2021. Investigating the subsurface in a shallow water environment using array and single-station ambient vibration techniques, *Geophys. J. Int.,* **227,** 1857–1878.

Spica, Z.J., Perton, M., Nakata, N., Liu, X. & Beroza, G.C., 2018. Site characterization at Groningen gas field area through joint surface-borehole H/V analysis, *Geophys. J. Int.,* **212,** 412–421.

Thomson, W.T., 1950. Transmission of elastic waves through a stratified solid medium, *J. Appl. Phys.,* **21,** 89–93.

Tian, Y. & Ritzwoller, M.H., 2015. Directionality of ambient noise on the Juan de Fuca plate: implications for source locations of the primary and secondary microseisms, *Geophys. J. Int.,* **201,** 429–443.

Tian, Y. & Ritzwoller, M.H., 2017. Improving ambient noise cross-correlations in the noisy ocean bottom environment of the Juan de Fuca plate, *Geophys. J. Int.,* **210,** 1787–1805.

Tokimatsu, K., Tamura, S. & Kojima, H., 1992. Effects of Multiple Modes on Rayleigh Wave Dispersion Characteristics, *Journal of Geotechnical Engineering,* **118**(10), 1529–1543.

Tsuru, T., Park, J.-O., Miura, S., Kodaira, S., Kido, Y. & Hayashi, T., 2002. Along-arc structural variation of the plate boundary at the Japan Trench margin: implication of interplate coupling, *J. geophys. Res. Solid Earth,* **107,** ESE 11–11-ESE 11-15.

Tuan, T.T., Vinh, P.C., Ohrnberger, M., Malischewsky, P. & Aoudia, A., 2016. An improved formula of fundamental resonance frequency of a layered half-space model used in H/V ratio technique, *Pure appl. Geophys.,* **173,** 2803–2812.

Vassallo, M., Festa, G. & Bobbio, A., 2012. Seismic ambient noise analysis in southern Italy, *Bull. seism. Soc. Am.,* **102,** 574–586.

Vella, A., Galea, P. & D'Amico, S., 2013. Site frequency response characterisation of the Maltese islands based on ambient noise H/V ratios, *Eng. Geol.,* **163,** 89–100.

Wathelet, M., 2008. An improved neighborhood algorithm: parameter conditions and dynamic scaling, *Geophys. Res. Lett.,* **35,** 1–5.

Wathelet, M., Chatelain, J.L., Cornou, C., Giulio, G. Di, Guillier, B., Ohrnberger, M. & Savvaidis, A., 2020. Geopsy: a user-friendly open-source tool set for ambient vibration processing, *Seismol. Res. Lett.,* **91,** 1878–1889.

Webb, S.C., 1998. Broadband seismology and noise under the ocean, *Rev. Geophys.,* **36,** 105–142.

Wu, H., Masaki, K., Irikura, K. & Sánchez-Sesma, F.J., 2017. Application of a simplified calculation for full-wave microtremor H/V spectral ratio based on the diffuse field approximation to identify underground velocity structures, *Earth Planets Space,* **69,** 162, doi: 10.1186/s40623-017-0746-8

Yamanaka, H., Takemura, M., Ishida, H. & Niwa, M., 1994. Characteristics of long-period microtremors and their applicability in exploration of deep sedimentary layers, *Bull. seism. Soc. Am.,* **84,** 1831–1841.

Yamaya, L., Mochizuki, K., Akuhara, T. & Nishida, K., 2021. Sedimentary structure derived from multi-mode ambient noise tomography with dense OBS Network at the Japan Trench, *J. geophys. Res. Solid Earth,* **126,** doi: 10.1029/2021JB021789

Zhao, D., Hasegawa, A. & Horiuchi, S., 1992. Tomographic imaging of *P*- and *S*-wave velocity structure beneath northeastern Japan, *J. geophys. Res. Solid Earth,* **97,** 19 909–19 928.

SUPPORTING INFORMATION

Supplementary data are available at *GJI* online.

Figure S1. Azimuthal variation analysis of the H/V ratios for all of the stations except those presented in Fig. 5.

Figure S2. PPSD plots of the H2 (North) components of three broadband stations.

Figure S3. H/V inversion results with misfit information and synthetic models generated for the stations of array AoA5, except for station AoA51 presented in Fig. 6. The observed and generated H/V curve models are presented in the top left-hand panel; misfit information is presented in the top right-hand panel (only misfits ranging from the lowest to a selected upper value are shown, and only the models associated with them are presented in the other panels); the best-fitting V_S with the generated models is presented in the bottom left-hand panel; and the best-fitting V_P with the generated models is presented in the bottom right-hand panel. mbsl: meter below sea level.

Figure S4. H/V inversion results with misfit information and synthetic models generated for the stations of array AoA6. The observed and generated H/V curve models are presented in the top left-hand panel; misfit information is presented in the top right-hand panel (only misfits ranging from the lowest to a selected upper value are shown, and only the models associated with them are presented in the other panels); the best-fitting V_S with the generated models is presented in the bottom left-hand panel; and the best-fitting V_P with the generated models is presented in the bottom right-hand panel. mbsl: meter below sea level.

Figure S5. H/V inversion results with misfit information and synthetic models generated for the stations belonging to array AoA7. The observed and generated H/V curve models are presented in the top left-hand panel; misfit information is presented in the top right-hand panel (only misfits ranging from the lowest to a selected upper value are shown, and only the models associated with them are presented in the other panels); the best-fitting V_S with the generated models is presented in the bottom left-hand panel; and the best-fitting V_P with the generated models is presented in the bottom right-hand panel. mbsl: meter below sea floor.

Figure S6. Water layer effect on the H/V curve from all OBS stations, except those presented in Fig. 10. Synthetic H/V obtained by removing the water layer from the best profile of the inversion result (dashed red line) compared with the H/V curve from the best profile with the water layer included (dashed blue line) and the observed H/V curve (solid green line).

Please note: Oxford University Press is not responsible for the content or functionality of any supporting materials supplied by the authors. Any queries (other than missing material) should be directed to the corresponding author for the paper.